

# Architected mesoporous crystalline magnesium silicates with ordered pore structures

Xun Gao <sup>a</sup>, Hassnain Asgar <sup>a</sup>, Ivan Kuzmenko <sup>c</sup>, Greeshma Gadikota <sup>a,b,\*</sup>

<sup>a</sup> School of Civil and Environmental Engineering, Cornell University, Ithaca, NY, 14853, USA

<sup>b</sup> Smith School of Chemical and Biological Engineering, Cornell University, Ithaca, NY, 14853, USA

<sup>c</sup> Advanced Photon Source, Argonne National Laboratory, Lemont, IL, 60439, USA



## ARTICLE INFO

### Keywords:

Crystalline mesoporous magnesium silicate  
Sol-gel synthesis  
Carbon coating  
Chemo-morphological coupling

## ABSTRACT

Novel approaches to harness earth abundant silicates as building blocks for carbon dioxide removal, capture, utilization, and storage are gaining increasing attention in the context of sustainable and low carbon energy and resource recovery. Advancing a calibrated understanding of these fluid-silicate interactions is essential for developing scalable processes. One of the challenges in developing predictive controls over these interactions is the compositional and morphological heterogeneity of naturally occurring, heterogeneous magnesium silicate minerals. To address this challenge, the synthesis of architected mesoporous crystalline magnesium silicate ( $Mg_2SiO_4$ ) is proposed. While synthesis routes for producing amorphous mesoporous magnesium silicates have been developed via sol-gel methods, approaches to synthesize crystalline magnesium silicates with well-controlled pore size distributions have not been explored. The conventional approaches of converting matter that is amorphous to crystalline states at elevated temperatures results in a heterogeneous pore size distribution. To develop controls on pore size distribution, amorphous mesoporous magnesium silicates are coated with carbon. This approach retains the pore structure during the amorphous to crystalline transformations of Mg-silicates at elevated temperatures. The carbon coating is removed on heating. Magnesium silicate particles produced using this approach have highly ordered pores around 2.58 nm and a specific surface area of 124.25  $m^2/g$ . In this study, we report the chemical compositions, morphologies, phase transitions, and pore structures of the intermediate materials produced during the synthesis of crystalline mesoporous magnesium silicates. The synthesis routes discussed in this study can be applied translationally to produce metal silicates with ordered mesoporous structures.

## 1. Introduction

As we transition to sustainable and renewable energy resources, our dependence on metals is expected to increase significantly. The need for metal-based electrodes for electrolysis to produce fuels and clean water, catalysts for energy and resource conversion, and rare earths for electronic materials is the societal basis for exploring earth-abundant and low-value substrates for metal recovery and utilization. In this context, naturally occurring magnesium silicates are receiving increasing attention since they are a source of nickel and iron, and are a source of magnesium for  $CO_2$  capture, storage, and removal [1–8]. Earth-abundant magnesium silicate minerals include  $(Mg, Fe)_2SiO_4$  (olivine) and serpentine  $((Mg, Fe)_3Si_2O_5(OH)_4$ ). Without any pre-treatment, olivine is considered to be more reactive compared to

serpentine. The magnesium end member of olivine is  $Mg_2SiO_4$  (forsterite) and the iron end member is  $Fe_2SiO_4$  (fayalite). Olivine is being extensively investigated for  $CO_2$  removal via weathering [9–11] and carbon mineralization [1–8,12–18].

In enhanced weathering, the dissolution of magnesium silicates releases  $Mg^{2+}$  ions. Each  $Mg^{2+}$  ion can capture two molecules of  $CO_2$  from air to produce two bicarbonate ions in soils and enhance soil fertility for crop production and growth. In carbon mineralization, magnesium (or calcium) silicates are reacted with  $CO_2$  to produce magnesium (or calcium) carbonates [1,2,4–8,12–18]. The chemical and morphological heterogeneity of naturally occurring Mg-silicates, anomalous speciation behavior that is highly sensitive to pH, temperature, gas compositions, and ionic strength, and the ambiguous role of precipitated silica on the reactivity of Mg-silicates [1,12,19–22]. These challenges motivate the

\* Corresponding author. School of Civil and Environmental Engineering, Cornell University, Ithaca, NY, 14853, USA.

E-mail address: [gg464@cornell.edu](mailto:gg464@cornell.edu) (G. Gadikota).

synthesis of mesoporous magnesium silicates with well-ordered pore structures to advance a calibrated understanding of the synthesis of magnesium silicates.

These studies will have a translational impact on the use of magnesium silicates for several industrial and medical applications. First, silicate materials are ideal adsorbents for wastewater filtration systems. For example, silicate materials can be used to adsorb phosphate, fluoride, cobalt salt, ammonia nitrogen, heavy metal ions, and organic pollutants [23–28]. Silicate materials also play important roles in manufacturing long-lasting phosphor and plasma display panels (PDPs) [29,30]. Moreover, because of the extremely low electrical conductivities and dielectric constants of some silicate materials, they are often used in electrical or micro-wave devices. In the medical industry, magnesium silicates are used in drug delivery, protein adsorption, and bone regeneration [31–33]. These widespread applications of magnesium silicates motivate the design of novel synthesis routes for producing crystalline magnesium silicates with mesoporous structures.

Prior work has been focused on the synthesis of magnesium silicates such as  $Mg_2SiO_4$  and  $MgSiO_3$  using sol-gel, hydrothermal, and ball-milling methods. Sanosh and coworkers [34] reported a sol-gel method to synthesize amorphous  $Mg_2SiO_4$  nanoparticles with a narrow particle size distribution of approximately 27 nm. Magnesium nitrate hexahydrate ( $Mg(NO_3)_2 \cdot 6H_2O$ , MNH) and tetraethyl ortho-silicate (TEOS) were used as sources of magnesium and silicate, respectively. The reaction was performed in an acidic environment, and the final product had a prolate spheroidal structure [34]. Ni and coworkers [35] synthesized forsterite ceramics with high bending strength and fracture toughness using sol-gel methods. This study used magnesium nitrate hexahydrate ( $Mg(NO_3)_2 \cdot 6H_2O$ ) and colloidal  $SiO_2$  as starting materials to produce a gel that was subsequently calcined [35]. Similarly, Kharazia and coworkers [36] used the same starting materials of sucrose and polyvinyl alcohol polymer (PVA) to form bioactive forsterite ceramic with a high surface area [36].

A template-assisted hydrothermal method was used to generate mesoporous magnesium silicate with a hierarchical structure [37]. In this approach, carbon-coated SBA-15 was used as a template. The pore walls of the template were transformed into crystalline magnesium silicate ( $Mg_3Si_4O_9(OH)_4$ ) [37] on heating. As an alternative to chemical routes, nanosized magnesium silicates [38] were synthesized using mechanical activation approaches without the liquid phase. Tavangarian and coworkers [39] synthesized single-phase nanocrystalline forsterite via two different ball-milling methods. In the first route, moderate talc ( $Mg_3Si_4O_10(OH)_2$ ) and magnesium carbonate ( $MgCO_3$ ) powders were mixed in a steel vial with steel balls and calcined after milling. By adjusting the ball-to-powder weight ratio, rotation speed, and calcination temperature, nanocrystalline forsterite powder with a particle size of approximately 40 nm was obtained [39]. The other ball-milling method replaces magnesium carbonate ( $MgCO_3$ ) powder with periclase ( $MgO$ ), producing a single-phase nanocrystalline forsterite [40].

Further, approaches to synthesize  $MgSiO_3$  (enstatite) were reported. Tsai and coworkers [41] developed a nanocrystalline enstatite fiber via the sol-gel method. In a typical synthesis procedure, they mixed tetraethoxysilane (TEOS) and a methanol solution of magnesium methoxide ( $Mg(OCH_3)_2$ ), followed by DI-water and acetic acid to promote the hydrolysis. After drying and calcination, the enstatite fibers were obtained [41]. In addition, Song and coworkers [42] reported the synthesis of  $MgSiO_3$  ceramics with good microwave dielectric properties via the ball-milling method. In this pathway,  $MgO$  and  $SiO_2$  powder were added to a nylon vial with zirconia balls for ball milling. The mixed powder was then calcined and ball-milled again. The final product was obtained by sintering the hydraulically pressed pellets from secondary ball milling [42].

In addition to amorphous  $Mg_2SiO_4$  and  $MgSiO_3$  materials, the synthesis of magnesium silicate hydroxide ( $Mg_3Si_2O_5(OH)_4$ ) and talc ( $Mg_3Si_4O_10(OH)_2$ ) has been explored. Magnesium silicate hydroxide ( $Mg_3Si_2O_5(OH)_4$ ) can be used as a lubricant additive. Zhuang and

coworkers [43] synthesized  $Mg_3Si_2O_5(OH)_4$  with different morphologies via the hydrothermal method. The researchers mixed  $Mg(NO_3)_2$ , ethanol, and PEG200, and added the mixture to  $Na_2SiO_3$  solution to precipitate  $Mg_3Si_2O_5(OH)_4$ . The precipitates were hydrothermally treated with  $NaOH$  solution to obtain the final product. By adjusting the concentration of  $NaOH$ , the morphology of the final product evolved from a hollow sphere to a core-shell sphere. Magnesium silicate nanotubes were produced by adding ethylene glycol at the end of the synthesis route [43]. Wang and coworkers [44] also produced magnesium silicate hydroxide with different morphologies and structures by hydrothermally treating  $MgO$  and  $SiO_2$  in  $NaOH$  solution. Talc ( $Mg_3Si_4O_10(OH)_2$ ), which is widely used to manufacture ceramics, paper, and paints, was synthesized with varying morphologies to meet industrial requirements [45]. Wang and coworkers [27] successfully used colloidal silica as a chemical template to synthesize  $Mg_3Si_4O_10(OH)_2$  hollow spheres. Moreover, Golubeva et al. [46] used the hydrothermal method to synthesize  $Mg_3Si_4O_10(OH)_2 \cdot nH_2O$  with an approximate particle size of 100 nm [46].

The application and performance of silicate materials greatly depend on the chemical compositions, structures, and morphologies of the particles. Mesoporous silicates are among the most attractive materials because of their excellent performance in adsorption, catalysis, molecular sieving, sensors, and electrochemistry [47]. According to IUPAC classification, mesoporous materials have a pore size between 2 nm and 50 nm [48]. Unlike traditional microporous materials synthesized by a single molecular template, the synthesis of mesoporous materials requires the participation of aggregated surfactant molecules as a template [49]. This type of aggregated molecular template is known as micelles, which form spontaneously when the surfactant concentration attains a critical value [50]. With templates, the desired materials can be synthesized outside, and the mesoporous structure is obtained after removing the micelles template by calcination or chemical extraction [47]. By applying proper surfactant concentrations, the size and structure of micelles can be controlled, which gives control over the shape and size of the pores in the final product. The wide-ranging applications and controllable structures of mesoporous magnesium silicate materials have attracted scientific attention. Specific examples are discussed below.

Lu and coworkers synthesized a crystalline  $Mg_3Si_4O_9(OH)_4$  using mesoporous silica as a template. In their study, they used SBA-15 as a template and silica source to form magnesium silicate via the hydrothermal method [51]. Zhu and coworkers synthesized amorphous mesoporous  $Mg_2SiO_4$  via the sol-gel method with surfactants [52]. These studies indicate that several varieties of magnesium silicate materials can be manufactured in a mesoporous structure. However, these approaches produce either amorphous magnesium silicates mesoporous materials or crystalline magnesium silicates that are not  $Mg_2SiO_4$ . Crystalline materials with mesoporous structures are preferred because of their better performance in targeted applications. Compared to amorphous products, crystalline materials possess better mechanical and thermal stabilities because of the long-range order of the molecules and the lattice defects [53]. Crystalline phases enhance optical, electronic, and photocatalytic activities in mesoporous materials [54]. Amorphous materials are typically transformed into crystalline matter using heat. Nevertheless, the mesoporous structure tends to collapse when amorphous Mg-silicate is heat-treated to produce crystalline phases. For this reason, prior studies have not attempted to tackle the challenge of producing crystalline  $Mg_2SiO_4$  with ordered pore structures.

To address this challenge, we developed a novel synthesis method to produce crystalline mesoporous forsterite ( $Mg_2SiO_4$ ) with narrow pore size distribution which is reported in this study. This method generates an amorphous mesoporous magnesium silicate precursor initially, followed by the amorphous-crystalline transition of the precursor in the presence of sucrose which is coated on the pore walls to maintain the pore structure. This sucrose coating inside the pores prevents the

collapse of the mesopores during the thermal treatment. The resulting crystalline matrix preserves the highly ordered pore structure.

To test the hypothesis that high purity mesoporous crystalline  $Mg_2SiO_4$  materials with ordered mesoporous structures can be synthesized using this route, we addressed the following research questions in this study: (i) Starting from amorphous  $Mg_2SiO_4$  gels, what is the chemical and morphological evolution of the materials as crystalline  $Mg_2SiO_4$  phases are formed? (ii) How do the pore volume and pore size distribution evolve during the various stages involved in the synthesis approaches? (iii) What are the mechanisms underlying the transition of amorphous to crystalline transition of  $Mg_2SiO_4$  in the presence of sucrose for maintaining the mesoscale porosity in these materials? To address these questions, the detailed material synthesis approaches, and the results from the characterization of these materials are discussed in the following sections.

## 2. Materials and method

### 2.1. Synthesis of crystalline mesoporous magnesium silicate

The reagents used in the study, Pluronic® P123 (EG<sub>27</sub>PG<sub>61</sub>EG<sub>27</sub>), magnesium nitrate hexahydrate ( $Mg(NO_3)_2 \cdot 6H_2O$ ), and tetraethylorthosilicate (TEOS) was purchased from Sigma Aldrich and 12 M hydrochloric acid (HCl) was acquired from Fisher Scientific. Sucrose was supplied by VWR, and sulfuric acid ( $H_2SO_4$ ) was procured from Ricca. Crystalline mesoporous magnesium silicates with highly ordered pores were developed using a multi-step synthesis route as shown in Fig. 1. The first step involves the synthesis of amorphous magnesium silicate via a sol-gel approach, followed by the preservation of pores using a carbon-coating approach, and finally, the removal of carbon and the formation of crystalline magnesium silicate.

In the first step, amorphous magnesium silicate was prepared by adding 3 g of P123 to 120 mL of 2 M HCl and 30 mL of DI water. The mixture was then stirred at 38 °C for 1 h, followed by the addition of 8.5

g of TEOS and 10.3 g of  $Mg(NO_3)_2 \cdot 6H_2O$ . This mixture was further stirred for 24 h at 38 °C. The precipitates generated during the first step were dried at 100 °C in the air for 24 h. P123 from within the pores was removed by calcining the dried sample at 600 °C at a ramping rate of 1 °C/min for 6 h in a benchtop muffle furnace (Thermo Scientific Thermolyne FB1410 M, Asheville, NC).

In the second step, the pores inside the amorphous mesoporous magnesium silicate obtained from Step 1 were coated and preserved using a carbon-coating approach. Typically, the direct thermal treatment of amorphous magnesium silicate produces crystalline magnesium silicates at temperatures higher than 800 °C, which results in the collapse of the mesopores. Since the overarching goal of this work is to develop the crystalline magnesium silicate with ordered pores, the carbon-coating route was chosen. In a typical coating procedure, 2 g of sucrose was dissolved in 0.224 g of  $H_2SO_4$  and 9.756 g of DI water. 1 g of amorphous magnesium silicate powder was added to this mixture and mixed at 120 °C for 12 h. In the next step, the sucrose coated magnesium silicate was calcined at 900 °C in nitrogen ( $N_2$ ) for 2 h at a ramp rate of 1 °C/min in the tube furnace (Lindberg Tube Furnace, 1000-C-1) to obtain crystalline magnesium silicate. The calcination step resulted in the carbon coating of pores and amorphous to the crystalline transformation of pore walls. In the final step, the carbon-coated sample was heated at 650 °C in the air for 3 h at a ramping rate of 20 °C/min using the benchtop muffle furnace to remove carbon from the pores [55]. As a reference, the as-synthesis amorphous magnesium silicate was calcined at 900 °C in nitrogen ( $N_2$ ) for 2 h at a ramp rate of 1 °C/min in the tube furnace to obtain the crystalline product without carbon coating.

### 2.2. Characterization of synthesized powders

The changes in the chemical composition and structure of synthesized samples were evaluated using infrared (IR) spectroscopy collected in an Attenuated Total Reflection (ATR) mode using an Attenuated Total Reflection-Fourier Transform Infrared spectrometer (ATR-FTIR,

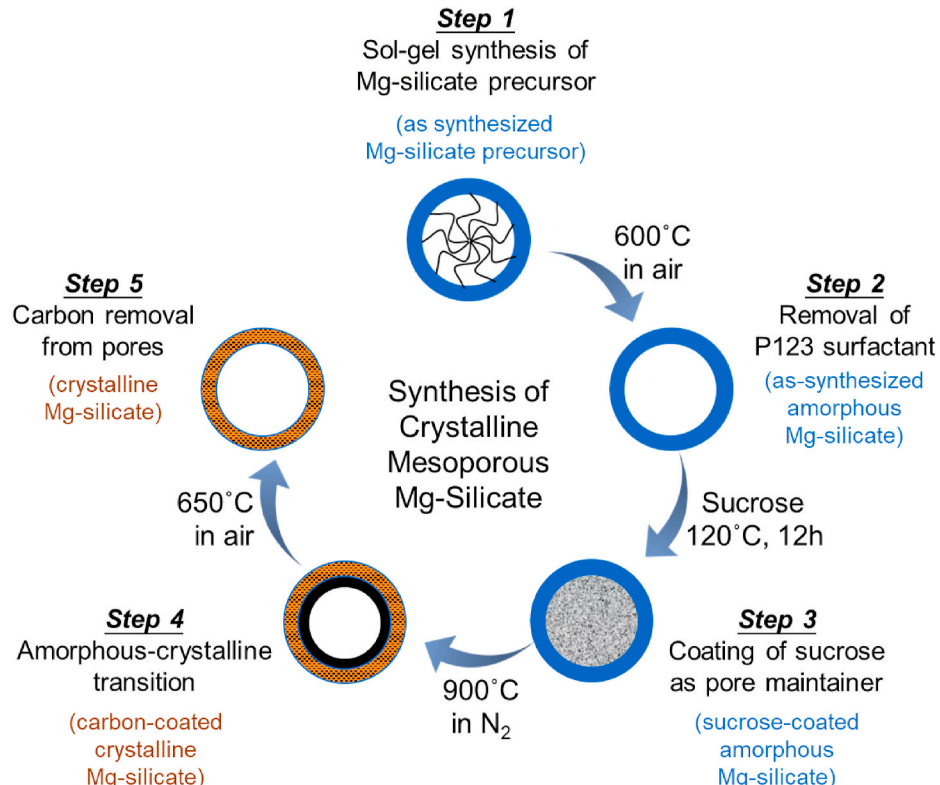


Fig. 1. Schematic representation of different stages of crystalline mesoporous magnesium silicate synthesis.

NicoletTM iS50, Waltham, MA) and the X-ray photoelectron spectroscopy (XPS, Scienta Omicron ESCA-2SR, Al K $\alpha$ ). The crystalline phases in the synthesized materials were obtained from X-ray diffraction (XRD, Bruker D8 Advance ECO powder diffractometer, Bruker). The morphology and particle size were determined by using field emission scanning electron microscopy (FESEM, LEO 1550 FESEM, Bruker) and field emission high resolution transmission electron microscope (FEI F20 TEM STEM) at 120 kV. Finally, the pore size distributions (PSD) were determined from N<sub>2</sub> adsorption-desorption isotherms using the Brunauer–Emmett–Teller technique (BET) (Quantachrome Autosorb iQ Analyzer, Boynton Beach, FL). Before measuring the adsorption-desorption isotherms, the synthesized samples were outgassed at 120 °C for 18 h.

Finally, the structural transitions during calcination in N<sub>2</sub> were determined using *in-situ* wide-angle X-ray scattering (WAXS) measurements between 30 °C and 906 °C in an N<sub>2</sub> environment. The measurements were performed in sector 9-ID-C at the Advanced Photon Source (APS), Argonne National Laboratory (ANL). The details about the instrument were reported in previous publications [56,57]. The sucrose-coated magnesium silicate sample was loaded into a quartz capillary (I.D. = 1.3 mm and O.D. = 1.5 mm) to acquire the scans. The background was taken from the empty capillary and subtracted from the data. During the acquisition, N<sub>2</sub> was also purged through the capillary. The X-ray energy was set to 21.0 keV, which corresponds to the X-ray wavelength of 0.59 Å. The total X-ray flux during the measurements was 10<sup>13</sup> photon mm<sup>-2</sup> s<sup>-1</sup>. The calibrations for sample-to-detector distance and instrument were performed using LaB<sub>6</sub>.

### 3. Result and discussion

#### 3.1. Chemical and structural changes during synthesis

As discussed in the previous section, the synthesis of crystalline magnesium silicate proceeds via sol-gel synthesis of amorphous Mg-silicate, followed by the coating of sucrose to maintain the pores in mesoporous in Mg-silicate, the transformation of amorphous Mg-silicate to crystalline Mg-silicate, and the removal of carbon which preserves the pores. Fig. 1 is a schematic representation of this approach. To evaluate the hypothesis that high purity crystalline magnesium silicate can be synthesized using this approach, the as-synthesized amorphous magnesium silicate, sucrose-coated magnesium silicate, carbon-coated magnesium silicate, and crystalline magnesium silicate are characterized in detail. For comparison, the as-synthesized magnesium silicate heat-treated without carbon-coating is also prepared and characterized.

The changes in the chemical bonding of these materials are determined using ATR FT-IR spectroscopy. The IR spectra identifying Si-O coordination are shown in Fig. 2. The peak corresponding to the asymmetric stretching vibrations of Si-O bonds around 1000 cm<sup>-1</sup> appeared in all the samples [58]. The peak representing Si-O-Si bending vibration around 650 cm<sup>-1</sup> is also noted in sucrose-coated magnesium silicate, carbon-coated magnesium silicate, and crystalline magnesium silicate [59]. Further, in the high wavenumber range (>2500 cm<sup>-1</sup>), the as-synthesized amorphous sample shows the Si-OH peak around 3200 cm<sup>-1</sup> and the peak of residual C-H bond from P123 at around 2980 cm<sup>-1</sup> [60,61,62]. The very low intensity indicates the small amount of the residual Si-OH bond and C-H in the sample. For the sucrose-coated sample, the strong OH peak appears around 3300 cm<sup>-1</sup> due to the hydroxyl (OH) functional groups in the sucrose molecules. Additionally, after the calcination in N<sub>2</sub> and air, the C-H bonds are eliminated. However, a weak signal from -OH bands around 3200 cm<sup>-1</sup> appears in the carbon-coated and crystalline samples, which could indicate the adsorbed moisture on the particles. On the other hand, the reference sample without a sucrose coat shows Si-O stretching peak at around 1050 cm<sup>-1</sup> and a Si-O-Si bending peak at around 850 cm<sup>-1</sup>, which can be a hint of the existence of MgSiO<sub>3</sub> [63]. Besides, the Si-O-Si peak around 950 cm<sup>-1</sup>, and Si-OH peak around 880 cm<sup>-1</sup> are also noted [58].

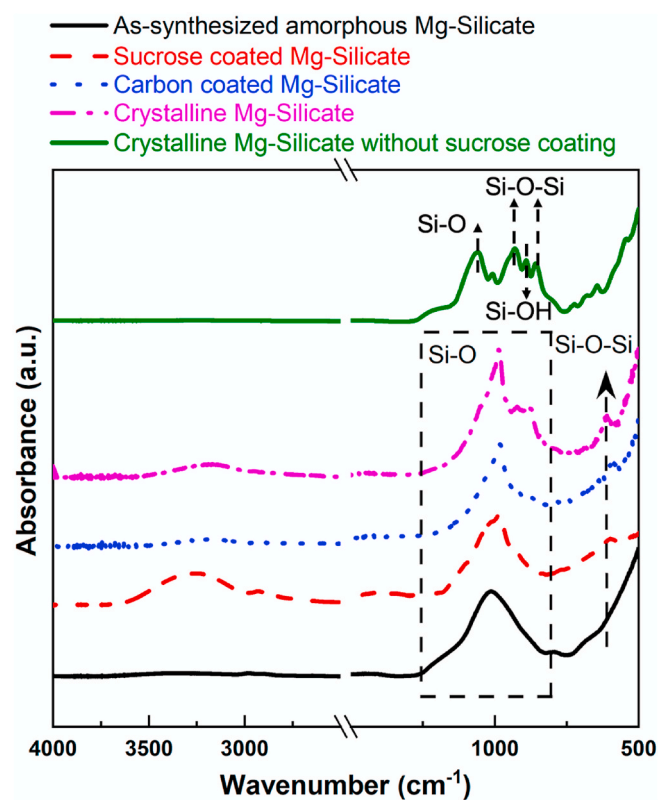
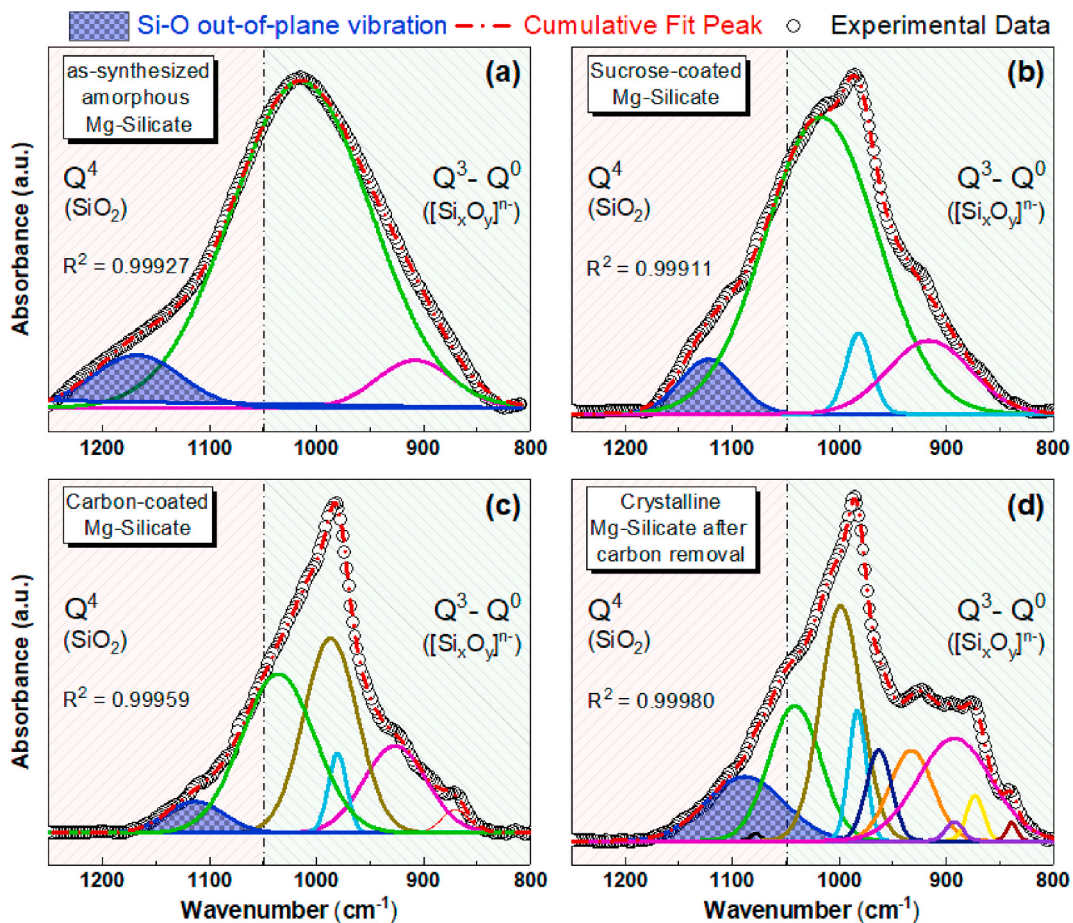


Fig. 2. Identification of different functional groups using Attenuated Total Reflection-Fourier Transform Infrared (ATR-FTIR) spectroscopy measurements in different mesoporous magnesium silicate samples.

Based on the IR spectra of the Si-O coordination, it can be noted that the peaks corresponding to the vibrations from Si-O linkages vary significantly across the different samples. To delineate the changes in the silica environment as the synthesis proceeds, the peaks that correspond to the Si-O bond between 1250 and 800 cm<sup>-1</sup> were deconvoluted (Fig. 3) using the Levenberg Marquardt algorithm with a Gaussian model embedded in Origin Pro software (OriginLab Corp.). The deconvolution provides information about the Q<sup>n</sup> coordination in silica during the synthesis. The Q<sup>n</sup> notation (n = 0, 1, 2, 3, 4) represents the number of bridging oxygens per Si tetrahedron in silicate-based materials [64]. Q<sup>4</sup> corresponds to SiO<sub>2</sub> species with 0 non-bridging oxygens (NBOs), while Q<sup>0</sup> represents 4 NBOs in [SiO<sub>4</sub>]<sup>4-</sup>-related species. The silicate species, corresponding Q<sup>n</sup> notations, NBOs, and wavenumber ranges (cm<sup>-1</sup>) are reported in Table 1.

For as-synthesized amorphous Mg-silicate, the main peaks corresponding to the amorphous silica (SiO<sub>4</sub>) with 0 non-bridging oxygens are expected due to the hydrolysis of TEOS in the acidic solution and condensation to form  $\equiv$ Si-O-Si $\equiv$  linkages (Fig. 3 (a)) [65–68]. Since the sol-gel synthesis conditions used in this study lead to the formation of amorphous silica linkages with Mg<sup>2+</sup> cations (from Mg(NO<sub>3</sub>)<sub>2</sub>) randomly distributed in the matrix, we noted a slight shift in the main peak, which appears  $\sim$ 1015 cm<sup>-1</sup> instead of the typical  $\sim$ 1080 cm<sup>-1</sup> peak for amorphous silica systems (SBA-15, Stöber silica particles, etc.) [63,64,69,70]. The presence of these cations could affect the NBOs in amorphous silica, as noted by a peak around 907 cm<sup>-1</sup> in Fig. 3 (a), corresponding to 3 NBOs with Q<sup>1</sup> coordination. In silicate-based materials, the segregation of [SiO<sub>4</sub>]<sup>4-</sup> tetrahedra upon sharing of an oxygen atom can lead to [SiO<sub>3</sub> – O – SiO<sub>3</sub>]<sup>6-</sup> species and free O<sup>2-</sup> ions that coordinate with Mg<sup>2+</sup> cations in the matrix and form MgO-based regions [71]. This observation is consistent with the formation of crystalline MgO peaks in the XRD patterns of as-synthesized Mg-silicate (Fig. 4).

After sucrose-coating on mesoporous Mg-silicate, the position of the



**Fig. 3.** Delineation of  $Q^4$ - $Q^0$  contributions from silicate species using deconvoluted ATR-IR spectra for as-synthesized (a), sucrose-coated (b), carbon-coated (c), and crystalline (d) Mg-silicate samples, respectively.

**Table 1**  
Classification of different silicate units and corresponding  $Q^n$  notations, non-bonding oxygens (NBOs), and wavenumber ranges.

$Q^n$ notation	Non-Bridging Oxygens (NBOs)	Unit	Wavenumber (cm <sup>-1</sup> )
$Q^4$	0	$SiO_2$	1300–1051
$Q^3$	1	$[Si_2O_5]^{2-}$	1050–981
$Q^2$	2	$[SiO_3]^{2-}$	980–951
$Q^1$	3	$[Si_2O_7]^{5-}$	950–901
$Q^0$	4	$[SiO_4]^{4-}$	900–850

**Table 2**  
Parameters extracted from  $N_2$  adsorption-desorption measurements using non-local density functional theory (NLDFT) model on the adsorption branch.

Sample ID	Average Pore Width (nm)	Surface Area (m <sup>2</sup> /g)	Pore Volume (cc/g)
As-synthesized amorphous Mg-silicate	6.56	276.35	0.43
Sucrose coated Mg-silicate	4.89	0.27	0.001
Carbon coated Mg-silicate	1.87	384.43	0.14
Crystalline Mg-silicate	2.58	124.25	0.12
Crystalline Mg-silicate without sucrose coating	4.89	9.53	0.03

$Si-O-Si$  remains unchanged around  $\sim 1015$  cm<sup>-1</sup> while a new peak is noted around 981.68 cm<sup>-1</sup>, which can result from the distortion in  $[SiO_4]^{4-}$  tetrahedra coordination during treatment in the presence of  $H_2SO_4$  and sucrose. Moreover, the  $MgO$  peaks in the XRD pattern of sucrose-coated Mg-silicate (Fig. 4 (b)) are also diminished, which may

result from the distortion of  $Mg-O$  coordination upon exposure to  $H_2SO_4$ -based solution. Thermal treatment of sucrose-coated Mg-silicate in the presence of  $N_2$  results in a significant change in the IR spectra and deconvoluted peaks, as depicted by the carbon-coated Mg-silicate sample (Fig. 3 (c)). As a result of thermal treatment, the amorphous silica ( $SiO_2$ ) linkages are transformed to a relatively high number of NBOs, which is an indication of  $[Si_xO_y]^{n-}$  species coordination with  $Mg^{2+}$  cations [71,72]. Finally, upon removal of carbon from Mg-silicate in the final heating stage, the number of peaks for  $[Si_xO_y]^{n-}$  species are significantly increased (Fig. 3 (d)), which may indicate increased coordination of  $Mg^{2+}$  cations with silicate species upon removal of carbon from the matrix. The higher peak counts in the XRD pattern of crystalline Mg-silicate after carbon removal compared to carbon-coated Mg-silicate also indicates the increased bonding between these species. Moreover, the shoulder peak for 'out-of-phase'  $Si-O$  stretching vibrations [73] noted for as-synthesized amorphous Mg-silicate at 1167.49 cm<sup>-1</sup> (blue curve, Fig. 3 (a)) is shifted to lower wavenumbers at 1121.35 cm<sup>-1</sup>, 1112.98 cm<sup>-1</sup>, and 1087.78 cm<sup>-1</sup> for sucrose-coated Mg-silicate (Fig. 3 (b)), carbon-coated Mg-silicate (Fig. 3 (c)), and crystalline Mg-silicate (Fig. 3 (d)), respectively. This shift of the out-of-phase shoulder peak to significantly lower wavenumber (cm<sup>-1</sup>) upon formation of completely crystalline Mg-silicate is consistent with the observation of the shoulder band for amorphous silica [67,68] and crystalline magnesium silicate products [74,75].

To further determine the variations in the chemical states during the synthesis, X-ray photoelectron spectroscopy (XPS) is also applied to magnesium silicate samples. The survey scans (Fig. 5) show O 1s, Si 2p, and Mg 2s peaks in the samples, which indicate the existence of  $O^{2-}$ ,  $Si^{4+}$ , and  $Mg^{2+}$  in these samples. The sucrose-coated and carbon-coated

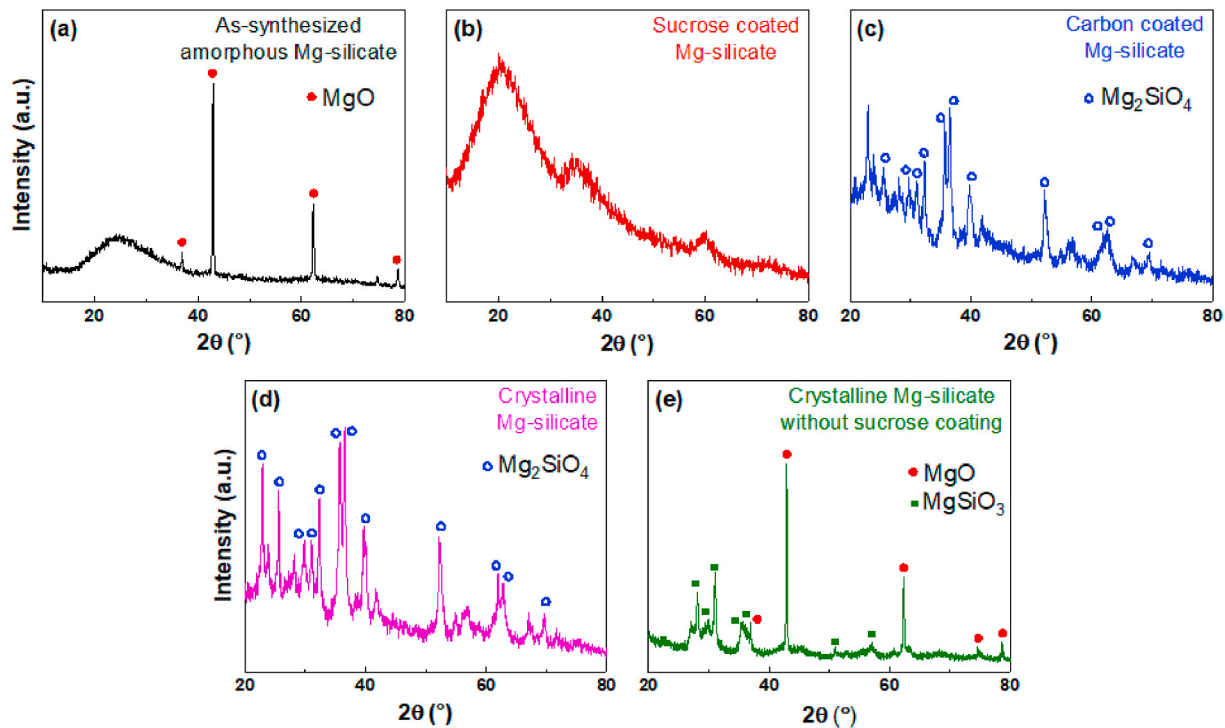


Fig. 4. Structural arrangement in as-synthesized amorphous magnesium silicate (a), sucrose-coated magnesium silicate (b), carbon-coated magnesium silicate (c), crystalline magnesium silicate (d), and crystalline magnesium silicate without sucrose coating (e) determined using X-ray diffraction.

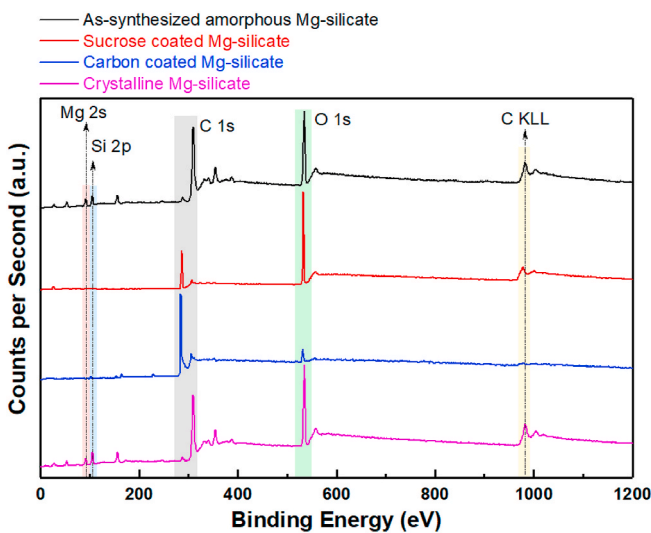
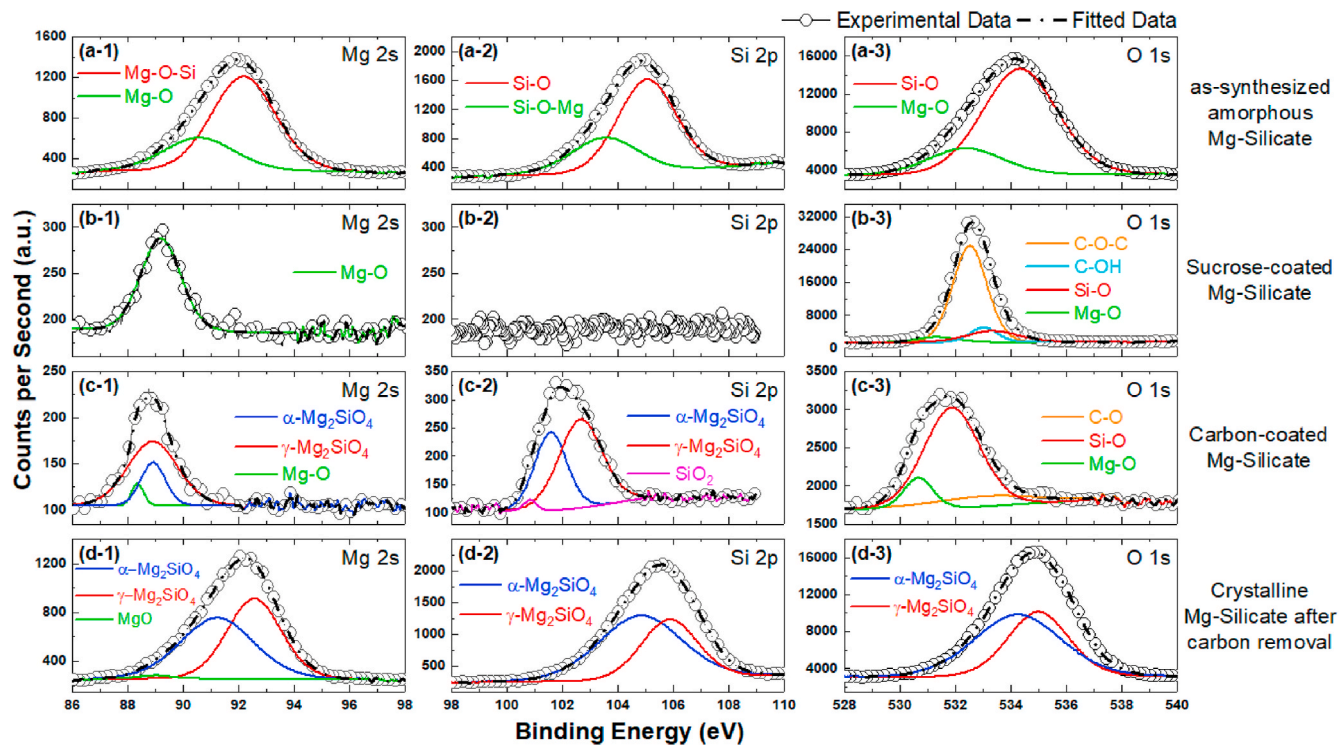


Fig. 5. Identification of magnesium, silicon, carbon, and oxygen peaks using X-ray photoelectron spectroscopy (XPS) spectra. (For interpretation of the references to colour in this figure legend, the reader is referred to the Web version of this article.)

magnesium silicate samples have C 1s peaks originating from sucrose and carbon, respectively, in these samples. Further, the high-resolution scans for individual elements (magnesium, silicon, oxygen, and carbon) are analyzed, which reveal the variations in the chemical states during synthesis of crystalline mesoporous magnesium silicate (Fig. 6 & Fig. S1). In the deconvoluted high-resolution spectra, the Mg 2s spectrum shows consistency with the others. The as-synthesized amorphous sample (Figs. 6 (a-1)) has Mg 2s peaks of Mg-O bond at 90.55 and Mg-O-Si bond at 92.16 eV [76,77]. And the crystalline magnesium silicate sample shows three different Mg 2s peaks at 88.98, 91.21, 92.55 eV, which represent the Mg-O bond, and the Mg-O-Si in different phases of

$\text{Mg}_2\text{SiO}_4$  (i.e.,  $\alpha\text{-Mg}_2\text{SiO}_4$  and  $\gamma\text{-Mg}_2\text{SiO}_4$ ), respectively. The Si 2p spectrum of as-synthesized amorphous (Figs. 6 (a-2)) sample can be identified as the Si-O peak at 105.04 eV and the Si-O-Mg peak at 103.53 eV, respectively. After sucrose coating (Figs. 6 (b-2)), the Si 2p is not noted, which could be an indication of complete covering of particles resulting in diminishing of signals from Si 2p. After the calcination in  $\text{N}_2$ , the crystalline magnesium silicate with carbon coating shows  $\text{SiO}_2$  peak at 100.81 eV [78],  $\alpha\text{-Mg}_2\text{SiO}_4$  peak at 101.57 eV, and  $\gamma\text{-Mg}_2\text{SiO}_4$  peak at 102.64 eV, where the  $\gamma\text{-Mg}_2\text{SiO}_4$  is transferred from  $\alpha\text{-Mg}_2\text{SiO}_4$  at high temperatures [79–81]. Furthermore, the Si 2p spectrum of the final crystalline product also shows the  $\alpha\text{-Mg}_2\text{SiO}_4$ , and  $\gamma\text{-Mg}_2\text{SiO}_4$  peaks at 104.81, and 105.85 eV, respectively. On the other hand, the O 1s spectrum for the as-synthesized amorphous sample shows the Si-O peak at 534.33 eV, the Mg-O peak at 532.37 eV, which is consistent with the XRD results [79,82–84]. And for the O 1s spectra of the sucrose coated sample (Figs. 6 (b-3)), there are also C-O-C peak at 532.53 eV and C-OH peak at 533.02 eV other than the Si-O peak at 533.33 eV, and a very weak band of Mg-O bond at 531.33 eV [85,86]. After the calcination in  $\text{N}_2$ , the carbon-coated sample (Figs. 6 (c-3)) shows Mg-O peak at 530.67 eV, Si-O peak at 531.88 eV, and a weak C-O peak at 533.05 eV, respectively [79]. The results are verified by the Si 2p spectra and C 1s spectra for the same sample. Then, the O 1s spectrum of the crystalline magnesium silicate sample also can be deconvoluted into  $\alpha\text{-Mg}_2\text{SiO}_4$  peak at 534.25 eV, and  $\gamma\text{-Mg}_2\text{SiO}_4$  at 535 eV. The positive binding energy shift in the crystalline sample (Figs. 6 (d-3)) can result from the variational covalency of the oxygen bonds in the sample, which is caused by the calcination in the air [87]. Furthermore, the C 1s high-resolution deconvoluted peaks are presented in Fig. S1. As-synthesized amorphous Mg-silicate (Fig. S1 (a)) and crystalline Mg-silicate (Fig. S1 (d)) have signals from adventitious carbon, which is a carbonaceous layer outside the sample formed by the exposure to air [88]. In the case of sucrose-coated Mg-silicate (Fig. S1 (b)), peaks from the C-O-C bond, C-C bond, and C-OH bond are noted at 287.63, 284.58, and 286.14 eV, respectively [85,89]. Additionally, the carbon-coated Mg-silicate (Fig. S1 (c)) shows a strong C-C peak at 284.16 eV, which is deconvoluted into  $\text{sp}^2$  bonded,  $\text{sp}^3$  bonded peaks. The shoulder peak around



**Fig. 6.** Identification of changes in the chemical states of magnesium (a-1 to d-1), silicon (a-2 to d-2), and oxygen (a-3 to d-3) via deconvolution of Mg 2s, Si 2p, and O 1s peaks in as-synthesized amorphous, sucrose-coated, carbon-coated (c), and crystalline magnesium silicate samples, respectively. (For interpretation of the references to colour in this figure legend, the reader is referred to the Web version of this article.)

285.56 eV is identified as the C-O-C peak.

Combined with the FTIR data, the XPS results provide detailed variations of the compositions and chemical bonds in the Mg-silicate samples. For the as-synthesized amorphous sample, the Si-O-Si linkages from amorphous  $\text{SiO}_2$  are verified by both of the characterizations, while the XPS peak also indicates the existence of the Mg-O bond, supported by the crystalline MgO characteristic peaks in the XRD curve. For the sucrose-coated sample, the XPS signal of the Si and Mg peak is too weak to analyze due to the excess of sucrose in the sample, while the C 1s peaks of this sample reveal the presence of the sucrose coat. On the other hand, the FTIR results indicate the presence of  $\text{H}_2\text{SO}_4$  can distort the Mg-O and  $[\text{SiO}_4]^{4-}$  coordination. Then, during the calcination in  $\text{N}_2$ , the FTIR peaks show that the  $\text{Mg}^{2+}$  cations started to coordinate with  $[\text{Si}_x\text{O}_y]^{n-}$  ligands and form crystalline magnesium silicate, which is confirmed by the Si 2p peak of the crystalline  $\text{Mg}_2\text{SiO}_4$  in different phases. Finally, after the removal of the carbon coat, the increasing peak number of the  $[\text{Si}_x\text{O}_y]^{n-}$  species represents more Mg cations coordinate with  $[\text{Si}_x\text{O}_y]^{n-}$  and higher crystallinity, supported by the shifted Si 2p peaks and O 1s peaks of the  $\alpha\text{-Mg}_2\text{SiO}_4$  and  $\gamma\text{-Mg}_2\text{SiO}_4$ .

The structural features of crystalline magnesium silicates are determined using XRD as shown in Fig. 4. In the as-synthesized amorphous magnesium silicate (Fig. 4 (a)), the characteristic peaks of magnesium oxide (MgO) are noted [90], along with the wide peak between 15° and 35°, indicating the presence of amorphous  $\text{SiO}_2$  [91]. The MgO could be formed in the as-synthesized Mg-silicate upon calcination (at 600 °C) due to the coordination between  $\text{Mg}^{2+}$  cations and  $[\text{Si}_2\text{O}_7]^{6-}$  species. To reveal the morphology of the as-synthesized Mg-silicate sample further, the crystallite size of the generated MgO is calculated from the XRD data by the Scherrer equation [92,93]:

$$D = \frac{K \cdot \lambda}{B(2\theta) \cdot \cos\theta} \quad (1)$$

where D is the average crystallite size, K is the Scherrer constant, which is equal to 0.94 for spherical crystals with cubic symmetry,  $\lambda$  is the

wavelength of the applied X-ray, which is 0.154 nm in our case,  $2\theta$  is the Bragg angle, and  $B(2\theta)$  is the Full Width at Half Maximum (FWHM) in radians of the selected diffraction peak. In this work, the (200) peak of MgO is selected to calculate the crystallite size. From the peak center (42.89°) and the FWHM (0.0047 rad) of the diffraction peak (Fig. S2), the estimated crystallite size of the MgO in the as-synthesized Mg-silicate sample is 33.32 nm. After coating with sucrose, the characteristic peaks of MgO disappear (Fig. 4 (b)), which is attributed to the dissolution of MgO in the presence of  $\text{H}_2\text{SO}_4$  [94]. The broad peak around 22° indicates the presence of a complete amorphous phase in the sucrose-coated magnesium silicate sample. Furthermore, after the calcination in  $\text{N}_2$ , the characteristic peaks of  $\text{Mg}_2\text{SiO}_4$  emerge in the carbon-coated magnesium silicate sample (Fig. 4 (c)) [95]. The appearance of these characteristic peaks can be explained by the amorphous-to-crystalline transition of  $\text{Mg}_2\text{SiO}_4$ . During the thermal treatment, the bonds in amorphous magnesium silicate matrix rearrange to form crystalline and well-ordered  $\text{Mg}_2\text{SiO}_4$ . The thermal treatment in the presence of  $\text{N}_2$  serves two purposes here. First, it helps keep the carbon preserved inside the pores and avoids pore collapse during thermal treatment. Second, it results in the amorphous-to-crystalline transition of  $\text{Mg}_2\text{SiO}_4$ . In the final stage, after calcination at 650 °C and removal of carbon from the pores, the crystalline structure of  $\text{Mg}_2\text{SiO}_4$  is preserved (Fig. 4 (d)) [95]. For comparison, the XRD pattern of the crystalline sample without sucrose coating is also presented (Fig. 4 (e)). The characteristic peaks indicate that the sample consists of crystalline periclase (MgO) and enstatite ( $\text{MgSiO}_3$ ) instead of forsterite [96, 97]. The persistence of MgO in this sample after thermal treatment can be explained by the absence of sulfuric acid, present in the sucrose coating solution, which causes the dissolution of MgO. As a result, the MgO particles remain unaffected in the system and the rest of the matrix crystallizes as  $\text{MgSiO}_3$  [97]. The conclusion is also supported by the FTIR peaks of the crystalline sample without the sucrose coat we've discussed previously.

### 3.2. Particle and pore morphology of synthesized powders

To understand the morphological evolution during the synthesis process, the scanning electron micrographs shown in Fig. 7 are analyzed. The amorphous magnesium silicate forms cylindrical particles after the removal of P123 surfactant (Fig. 7 (a)), which is typical of particles prepared from similar sol-gel approaches [98]. After the sucrose coating, the particles are covered with the sucrose (Fig. 7 (b)). Upon calcination in  $N_2$ , the carbonization of sucrose resulted in the shrinkage of carbon around the particles in the carbon-coated magnesium silicate sample, resulting in cylindrical particles (Fig. 7 (c)). Based on the XRD pattern of the carbon-coated magnesium silicate sample, the particles after the calcination in  $N_2$  are crystalline and have similar morphology as the amorphous magnesium silicate. The morphology of crystalline magnesium silicate particles, after the final step of calcination in the air to remove the carbon, is also cylindrical (Fig. 7 (d)). With the comprehension of the particle morphology, we delineate the changes in the mesopores inside these cylindrical particles using the  $N_2$  adsorption-desorption measurements, as discussed below.

To verify that the final product has highly ordered pore sizes and reveal the variation in the pore sizes during the synthesis process, the BET  $N_2$  adsorption-desorption isotherms were measured at 77 K. The isotherms of the samples are shown in Fig. S3, and the pore size distribution curves of different samples are shown in Fig. 8. The pores size distributions from the isotherms are estimated using the non-local density functional theory (NLDFT) model, which is applied to the adsorption isotherm [99–101]. The as-synthesized amorphous magnesium silicate sample exhibits a type IV(a) isotherm having an H1 hysteresis (Fig. S3 (a)), typical of the uniform mesopores with a delayed condensation on the adsorption branch because of the capillary condensation in the pores [102]. The sucrose-coated magnesium silicate sample exhibited a random isotherm (Fig. S3 (b)). This can be explained by the occupation of pores by the sucrose molecules, which remain suspended in the pores and interrupt the capillary condensation phenomenon. However, the carbon-coated magnesium silicate shows type IV(a) isotherm with H2(a) hysteresis (Fig. S3 (c)) [102]. The type H2 hysteresis is exhibited by complex pore structures. The steep trend noted in the desorption branch can be attributed to pore-blocking in narrow pore necks or cavitation-induced evaporation [102]. The narrowing of

the pore neck occurs due to carbon-coating of the pores. After the removal of carbon to produce the final crystalline magnesium silicate product, type H3 hysteresis loop is noted as shown in Fig. S3 (d). The crystalline magnesium silicate without sucrose coating also exhibits a similar isotherm (Fig. S3 (e)). The distinctive features associated with the type H3 hysteresis loop are: (i) the resemblance of the adsorption branch to a type II isotherm and (ii) the lower limit of the adsorption branch, which is located at the cavitation-induced relative pressure ( $P/P_0$ ). Moreover, we did not observe any plateau at high  $P/P_0$  values, indicating that the isotherm for the crystalline magnesium silicate is not identified as type IV [102,103]. Besides having a resemblance to type II isotherm, the isotherm for crystalline magnesium silicate deviates from a true type II and can be characterized as pseudo-type II isotherm caused by the delayed capillary condensation. These features are characteristics of the presence of non-rigid aggregates, a low degree of pore curvature, and slit-like pores [102,104].

The surface areas of the amorphous magnesium silicate, sucrose-coated magnesium silicate, carbon-coated magnesium silicate, and crystalline magnesium silicate are  $276.35\text{ m}^2/\text{g}$ ,  $0.27\text{ m}^2/\text{g}$ ,  $384.43\text{ m}^2/\text{g}$ , and  $124.25\text{ m}^2/\text{g}$ , respectively (Table 2). The higher surface area exhibited by the as-synthesized amorphous magnesium silicate is attributed to the availability of pores resulting from surfactant removal from the mesoporous particles, and the high surface area of the carbon-coated sample comes from the porous carbon structure around the magnesium silicate particles. On the other hand, the pore volume for the as-synthesized amorphous magnesium silicate ( $0.43\text{ cc/g}$ ) is also larger than the sucrose coated ( $0.001\text{ cc/g}$ ), carbon-coated ( $0.14\text{ cc/g}$ ), and crystalline magnesium silicate ( $0.12\text{ cc/g}$ ) samples (Table 2). A significant decrease in the pore volume is noted after sucrose-coating, indicating the complete filling of mesopores. Conversely, carbon-coating via calcination in  $N_2$  increases the pore volume to  $0.14\text{ cc/g}$ . This increase can be explained by the pyrolysis of sucrose and the formation of carbon-coating along the pore walls (Fig. 1, step 4). Finally, after the removal of carbon from the pores by heating in air, the pore volume from the carbon structure is eliminated and the pore volume from the magnesium silicate decreases slightly, and the total pore volume reached a value of  $0.12\text{ cc/g}$ . The total pore volume and surface area of the crystalline magnesium silicate are lower than that of as-synthesized amorphous magnesium silicate. This observed decrease in the surface area and pore volume in

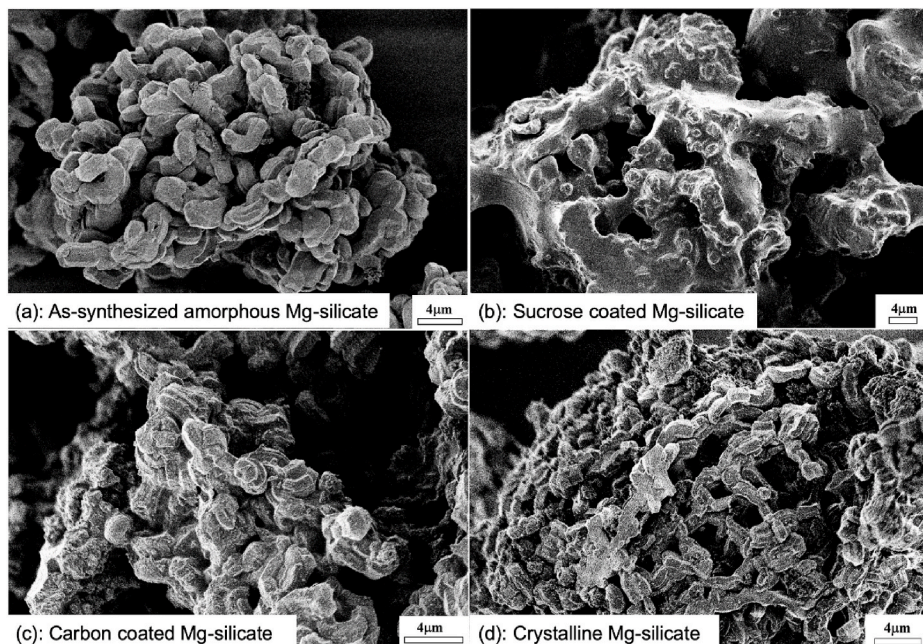


**Fig. 7.** Morphologies of amorphous (a), sucrose-coated (b), carbon-coated (c), and crystalline (d) mesoporous magnesium silicate samples determined using scanning electron micrographs (SEM).

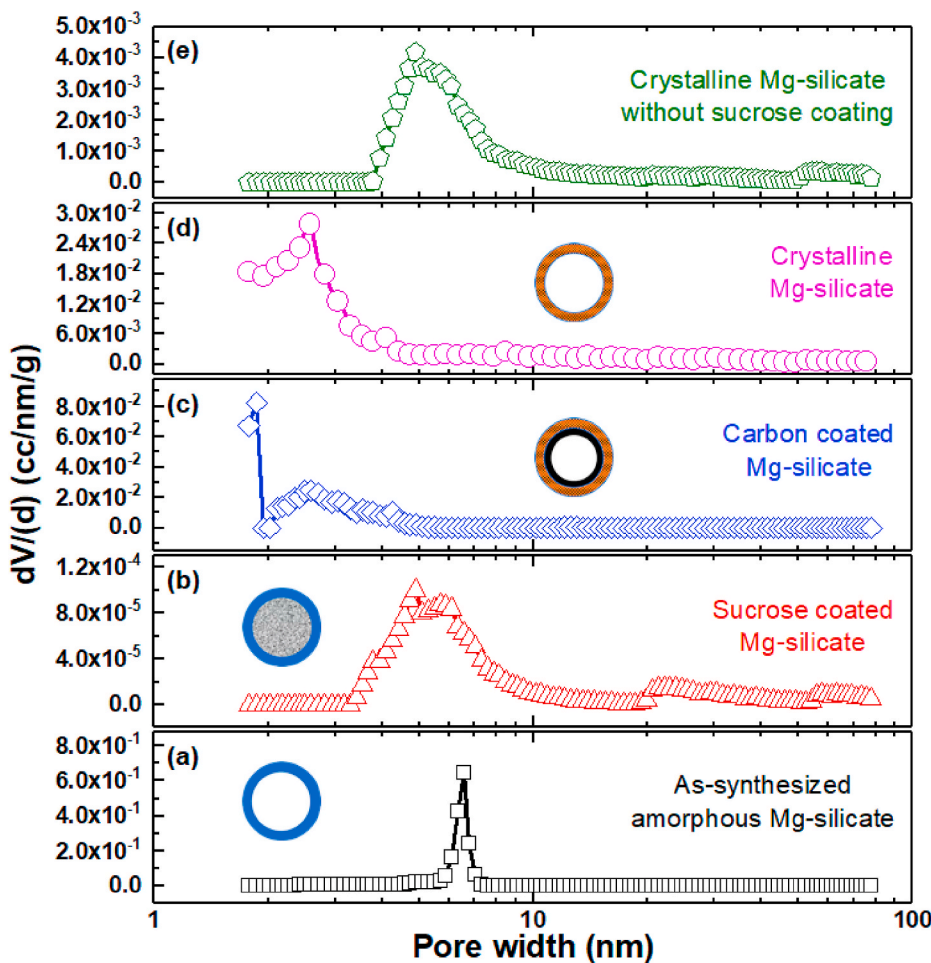


**Fig. 8.** Pore size distribution for as-synthesized amorphous magnesium silicate (a), sucrose-coated magnesium silicate (b), carbon-coated magnesium silicate (c), crystalline magnesium silicate (d) samples, and crystalline magnesium silicate without sucrose coating (e), respectively, determined using non-local density functional theory (NLDFT) model on the adsorption branch. The insets are schematic representations of the pores and the crystallinity of the pore walls.

crystalline magnesium silicate can be attributed to the densification of pore walls during amorphous-to-crystalline phase transformation. To be specific, the changes in the molecular attractions on heating to 900 °C cause amorphous phases to transform into crystalline phases [34]. The aggregation of particles causes the specific surface area to decrease during this amorphous to crystalline transformation. In mesoporous materials, heat treatment or sintering involves the collapse of the pore structure and aggregation of particles to decrease the surface free energy during calcination [105]. To prevent the collapse of the pore structure, magnesium silicate is coated with carbon. The mesoporous structure shrinks and densifies on heating instead of being eliminated which causes a small decrease in the pore volume.

The average pore sizes of as-synthesized amorphous magnesium silicate, carbon-coated magnesium silicate, and crystalline magnesium silicate are 6.56 nm, 4.89 nm, 1.87 nm, and 2.58 nm, respectively. The pore size distributions for as-synthesized amorphous magnesium silicate, sucrose-coated magnesium silicate, carbon-coated magnesium silicate, crystalline magnesium silicate, and crystalline magnesium silicate without sucrose coating are shown in Fig. 8 (a), (b), (c), (d), and (e), respectively. For as-synthesized amorphous magnesium silicate and crystalline magnesium silicate samples, narrow pore size distributions are noted, which are characteristic of highly ordered mesopores. As a precedent, Lu and coworkers have synthesized crystalline mesoporous  $Mg_3Si_4O_9(OH)_4$  with highly ordered pores around 3.8 nm by sucrose coating. However, they synthesized a magnesium silicate product via the hydrothermal method and the yield of the final product is relatively

limited [51]. In the case of carbon-coated magnesium silicate, when the sucrose pyrolysis coats carbon along with the pores of mesoporous structure, a variety of pore sizes (Fig. 8 (c)) are noted with an average value of 1.87 nm. This highlights a complex pore network formed in the mesoporous structure due to the carbon-coating, which is also indicated by the H2 type hysteresis for the carbon-coated magnesium silicate sample. On the other hand, the pore size distribution of the reference crystalline magnesium silicate without sucrose coating exhibits an average pore size and surface area of 4.89 nm, and 9.53  $m^2/g$ , respectively. However, the pore volume (0.03 cc/g) of this sample is significantly lower compared to other samples (Fig. 8 (e)), which indicates that most of the mesopores collapse during the calcination without the support of a carbon coat.

The pore size and crystalline arrangement of the pore walls in the crystalline magnesium silicate sample are visualized using high resolution transmission electron microscopy (HR-TEM) as presented in Fig. 9. The pore sizes around 2.6 nm are identified in the HR-TEM image. Moreover, the crystal orientation in the pore walls is observed from the lattice fringes and a d-spacing of 0.25 nm is noted, which corresponds to (311) plane of  $Mg_2SiO_4$  ( $\sim 2\theta = 36^\circ$ ) [95].

### 3.3. In-situ phase transitions during the transformations of amorphous to crystalline Mg-Silicates

The structural changes during the calcination of amorphous sucrose-coated magnesium silicate in  $N_2$  were evaluated using synchrotron-

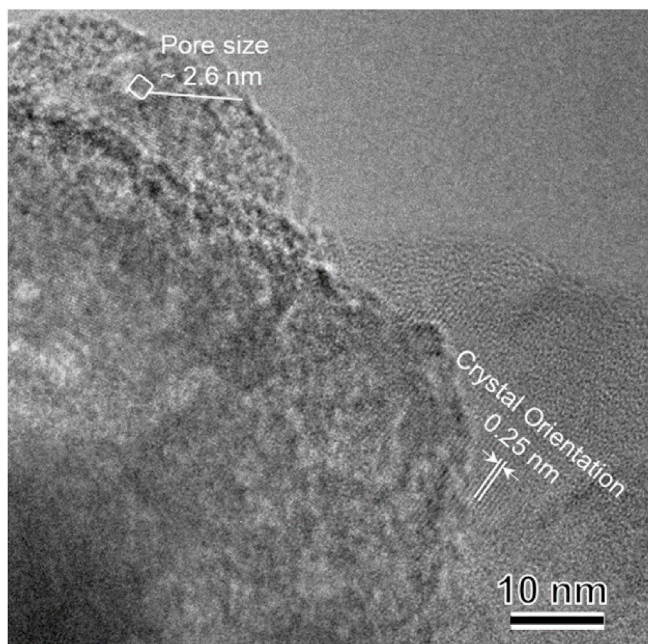


**Fig. 9.** Visualization of pore size and crystallinity in the pore walls for crystalline magnesium silicate sample determined using high-resolution transmission electron microscopy (HR-TEM).

based *in-situ* WAXS measurements. These measurements provide real-time insights into the phase transformations of the mesoporous matrix as a function of temperature. To reveal the phase transition process of the sucrose coated magnesium silicate sample during calcination, the evolution of (311) and (121) orientations of crystalline  $Mg_2SiO_4$  [95] are shown in Fig. 10. The entire WAXS patterns are shown in Fig. S4.

Initially, a relatively flat curve is noted at 30 °C, indicating an amorphous mesoporous matrix. The amorphous character of the matrix persists at higher temperatures (>500 °C), and the first emergence of the crystalline structure is noted at 779 °C. A continuous increase in the peak intensities of (311) and (121) orientations of crystalline  $Mg_2SiO_4$  [95] is noted till 906 °C. These observations are consistent with the transformation of amorphous to crystalline transformations of crystalline magnesium silicate. To summarize, the crystalline phases of magnesium silicate appear once temperatures higher than 779 °C are achieved.

#### 4. Conclusion

In this study, we report a novel route to synthesize crystalline magnesium silicate ( $Mg_2SiO_4$ ) with highly ordered mesopores starting from amorphous mesoporous magnesium silicate. The key challenge of preserving the pore diameter inside the mesopores range is resolved by coating the pores of amorphous magnesium silicates with sucrose followed by transforming these amorphous materials into crystalline phases and removing carbon by applying heat. The end product is crystalline and is composed of 100%  $Mg_2SiO_4$ . These particles have cylindrical morphologies, and the pore diameter is 2.58 nm. The highly ordered pore structures and large surface area of these materials make them ideal candidates for developing a calibrated understanding of the reactivity of these materials with  $CO_2$  for applications related to carbon capture, utilization, storage, and removal.

#### CRediT authorship contribution statement

**Xun Gao:** synthesized the materials and characterized the materials, Writing – original draft. **Hassnain Asgar:** contributed towards materials synthesis and characterization, Writing – original draft. **Ivan**

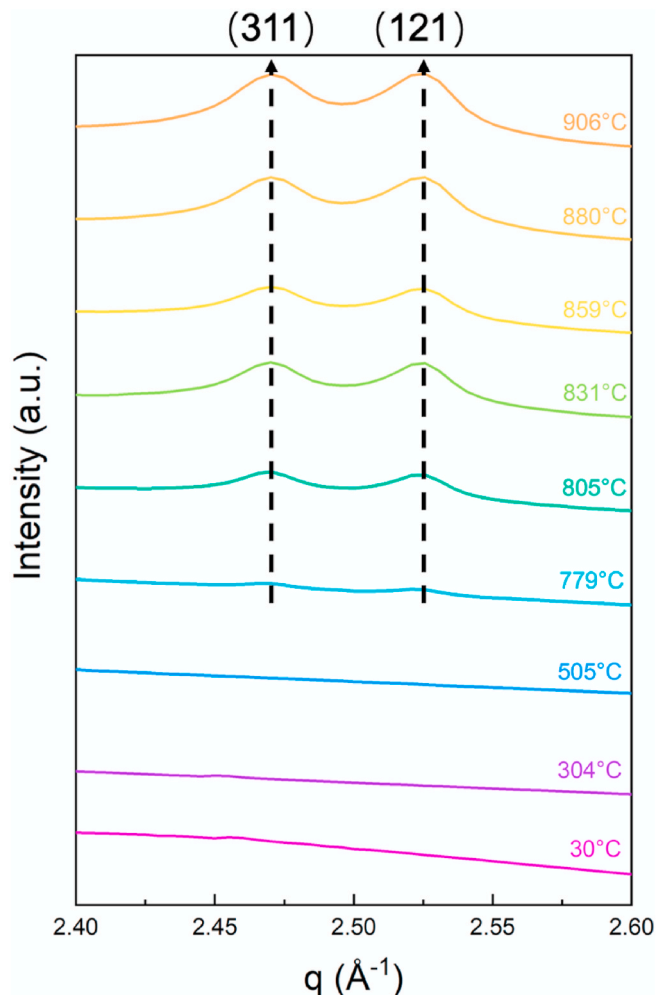


**Fig. 10.** Changes in the structural arrangements of the pore walls of mesoporous magnesium silicate samples were determined using *in-situ* Wide-Angle X-ray Scattering (WAXS) measurement.

**Kuzmenko:** supported synchrotron X-ray scattering measurements. **Greeshma Gadikota:** Writing – review & editing, Conceptualization.

#### Declaration of competing interest

The authors declare that they have no known competing financial interests or personal relationships that could have appeared to influence the work reported in this paper.

#### Acknowledgements

X. G. and G. G. are supported by the CAREER grant by the US Department of Energy, Office of Science, Basic Energy Sciences under the Award #DE-SC0020263. H. A. is supported by the EFRC-MUSE, an Energy Frontier Research Center funded by the U.S. Department of Energy, Office of Science, Basic Energy Sciences under Award #DE-SC0019285. The use of the Advanced Photon Source, an Office of the Science User Facility operated for the U.S. Department of Energy (DOE) Office of Science by Argonne National Laboratory, is supported by the U. S. DOE under Contract DE-AC02-06CH11357. This work made use of the Cornell Center for Materials Research (CCMR) Shared Facilities which are supported through the NSF MRSEC program (DMR-1719875), and the authors would like to acknowledge Dr. Darrah Johnson-McDaniel, who assisted with XPS measurements at CCMR. Besides, the authors gratefully acknowledge the support of Jan Ilavsky at APS and Akanksha

Srivastava at Cornell University for assisting this effort.

## Appendix A. Supplementary data

Supplementary data to this article can be found online at <https://doi.org/10.1016/j.micromeso.2021.111381>.

## References

- Gadikota, J. Matter, P. Kelemen, A.H.A. Park, Chemical and morphological changes during olivine carbonation for CO<sub>2</sub> storage in the presence of NaCl and NaHCO<sub>3</sub>, *Phys. Chem. Chem. Phys.* 16 (2014) 4679–4693, <https://doi.org/10.1039/c3cp54903h>.
- R.S. Miller, H.T. Schaeff, J.P. Kaszuba, G. Gadikota, B.P. McGrail, K.M. Rosso, Quantitative review of olivine carbonation kinetics: reactivity trends, mechanistic insights, and research frontiers, *Environ. Sci. Technol. Lett.* 6 (2019) 431–442, <https://doi.org/10.1021/acs.estlett.9b000301>.
- G. Gadikota, K. Fricker, S.-H. Jang, A.-H.A. Park, Carbonation of Silicate Minerals and Industrial Wastes and Their Potential Use as Sustainable Construction Materials, 2015, pp. 295–322, <https://doi.org/10.1021/bk-2015-1194.ch012>.
- G. Gadikota, Ah-Hyung A. Park, *Accelerated Carbonation of Ca- and Mg-Bearing Minerals and Industrial Wastes Using CO<sub>2</sub>*, Elsevier B.V., 2015.
- G. Gadikota, E.J. Swanson, H. Zhao, A.H.A. Park, Experimental design and data analysis for accurate estimation of reaction kinetics and conversion for carbon mineralization, *Ind. Eng. Chem. Res.* 53 (2014) 6664–6676, <https://doi.org/10.1021/ie500393h>.
- G. Gadikota, J. Matter, P. Kelemen, P.V. Brady, A.H.A. Park, Elucidating the differences in the carbon mineralization behaviors of calcium and magnesium bearing aluminosilicates and magnesium silicates for CO<sub>2</sub> storage, *Fuel* 277 (2020), 117900, <https://doi.org/10.1016/j.fuel.2020.117900>.
- G. Gadikota, Carbon mineralization pathways for carbon capture, storage and utilization, *Commun. Chem.* 4 (2021) 1–5, <https://doi.org/10.1038/s42004-021-00461-x>.
- M. Liu, G. Gadikota, Chemo-morphological coupling during serpentine heat treatment for carbon mineralization, *Fuel* 227 (2018), <https://doi.org/10.1016/j.fuel.2018.04.097>.
- L.L. Taylor, J. Quirk, R.M.S. Thorley, P.A. Kharecha, J. Hansen, A. Ridgwell, M. R. Lomas, S.A. Barnart, D.J. Beerling, Enhanced weathering strategies for stabilizing climate and averting ocean acidification, *Nat. Clim. Change* 6 (2016) 402–406, <https://doi.org/10.1038/nclimate2882>.
- D.J. Beerling, J.R. Leake, S.P. Long, J.D. Scholes, J. Ton, P.N. Nelson, M. Bird, E. Kantzias, L.L. Taylor, B. Sarkar, M. Kelland, E. DeLucia, I. Kantola, C. Müller, G. Rau, J. Hansen, Farming with crops and rocks to address global climate, food and soil security/631/449/706/1143/704/47/704/106 perspective, *Native Plants* 4 (2018) 138–147, <https://doi.org/10.1038/s41477-018-0108-y>.
- P.J. Frings, H.L. Buss, The Central Role of Weathering in the Geosciences, *Elements*, 15 (2019) 229–234, <https://doi.org/10.2138/geslements.15.4.229>.
- G. Gadikota, Multiphase carbon mineralization for the reactive separation of CO<sub>2</sub> and directed synthesis of H<sub>2</sub>, *Nat. Rev. Chem.* 4 (2020) 78–89, <https://doi.org/10.1038/s41570-019-0158-3>.
- G. Gadikota, Commentary: ex situ aqueous mineral carbonation, *Front. Energy Res.* 4 (2016), <https://doi.org/10.3389/fenrg.2016.00021>.
- W. Zhu, F. Fusseis, H. Lisabeth, T. Xing, X. Xiao, De Andrade, S.I. Karato, Experimental evidence of reaction-induced fracturing during olivine carbonation, *Geophys. Res. Lett.* 43 (2016) 9535–9543, <https://doi.org/10.1002/2016GL070834>.
- P.B. Kelemen, G. Hirth, Reaction-driven cracking during retrograde metamorphism: olivine hydration and carbonation, *Earth Planet Sci. Lett.* (2012) 345–348, <https://doi.org/10.1016/j.epsl.2012.06.018>, 81–89.
- A.N. Paukert, J.M. Matter, P.B. Kelemen, E.L. Shock, J.R. Havig, Reaction path modeling of enhanced in situ CO<sub>2</sub> mineralization for carbon sequestration in the peridotite of the Samail Ophiolite, Sultanate of Oman, *Chem. Geol.* (2012) 330–331, <https://doi.org/10.1016/j.chemgeo.2012.08.013>, 86–100.
- P.B. Kelemen, N. McQueen, J. Wilcox, P. Renforth, G. Dipple, A.P. Vankeuren, Engineered carbon mineralization in ultramafic rocks for CO<sub>2</sub> removal from air: review and new insights, *Chem. Geol.* 550 (2020), 119628, <https://doi.org/10.1016/j.chemgeo.2020.119628>.
- P.B. Kelemen, R. Aines, E. Bennett, S.M. Benson, E. Carter, J.A. Coggon, J.C. De Obeso, O. Evans, G. Gadikota, G.M. Dipple, M. Godard, M. Harris, J.A. Higgins, K. T.M. Johnson, F. Kourim, R. Lafay, S. Lambart, C.E. Manning, J.M. Matter, K. Michibayashi, T. Morishita, J. Noël, K. Okazaki, P. Renforth, B. Robinson, H. Savage, R. Skarbek, M.W. Spiegelman, E. Takazawa, D. Teagle, J.L. Urai, J. Wilcox, In situ carbon mineralization in ultramafic rocks: natural processes and possible engineered methods, *Energy Procedia* 146 (2018) 92–102, <https://doi.org/10.1016/j.egypro.2018.07.013>.
- D. Daval, O. Sissmann, N. Menguy, G.D. Saldi, F. Guyot, I. Martinez, J. Corvisier, B. Garcia, I. Machouk, K.G. Knauss, R. Hellmann, Influence of amorphous silica layer formation on the dissolution rate of olivine at 90°C and elevated pCO<sub>2</sub>, *Chem. Geol.* 284 (2011) 193–209, <https://doi.org/10.1016/j.chemgeo.2011.02.021>.
- H. Béarat, M.J. McKelvy, A.V.G. Chizmeshya, D. Gormley, R. Nunez, R. W. Carpenter, K. Squires, G.H. Wolf, Carbon sequestration via aqueous olivine mineral carbonation: role of passivating layer formation, *Environ. Sci. Technol.* 40 (2006) 4802–4808, <https://doi.org/10.1021/es0523340>.
- R. Hellmann, D. Daval, R. Wirth, formation of amorphous silica surface layers by dissolution-reprecipitation during chemical weathering: implications for CO<sub>2</sub> uptake, *Procedia Earth Planet. Sci.* 7 (2013) 346–349, <https://doi.org/10.1016/j.proeps.2013.03.154>.
- D. Daval, R. Hellmann, G.D. Saldi, R. Wirth, K.G. Knauss, Linking nm-scale measurements of the anisotropy of silicate surface reactivity to macroscopic dissolution rate laws: new insights based on diopside, *Geochem. Cosmochim. Acta* 107 (2013) 121–134, <https://doi.org/10.1016/j.gca.2012.12.045>.
- A. Renman, G. Renman, Long-term phosphate removal by the calcium-silicate material Polonite in wastewater filtration systems, *Chemosphere* 79 (2010) 659–664, <https://doi.org/10.1016/j.chemosphere.2010.02.035>.
- C.E. Choong, K.T. Wong, S.B. Jang, I.W. Nah, J. Choi, S. Ibrahim, Y. Yoon, M. Jang, Fluoride removal by palm shell waste based powdered activated carbon vs. functionalized carbon with magnesium silicate: implications for their application in water treatment, *Chemosphere* 239 (2020), 124765, <https://doi.org/10.1016/j.chemosphere.2019.124765>.
- G. Qi, X. Lei, L. Li, C. Yuan, Y. Sun, J. Chen, J. Chen, Y. Wang, J. Hao, Preparation and evaluation of a mesoporous calcium-silicate material (MCSM) from coal fly ash for removal of Co(II) from wastewater, *Chem. Eng. J.* 279 (2015) 777–787, <https://doi.org/10.1016/j.cej.2015.05.077>.
- Q. Si, Q. Zhu, Z. Xing, Design and synthesis of a novel silicate material from red mud for simultaneous removal of nitrogen and phosphorus in wastewater, *ACS Sustain. Chem. Eng.* 5 (2017) 11422–11432, <https://doi.org/10.1021/acssuschemeng.7b02538>.
- Y. Wang, G. Wang, H. Wang, C. Liang, W. Cai, L. Zhang, Chemical-template synthesis of micro/nanoscale magnesium silicate hollow spheres for waste-water treatment, *Chem. Eur. J.* 16 (2010) 3497–3503, <https://doi.org/10.1002/chem.200902799>.
- S. Zhang, W. Xu, M. Zeng, J. Lii, J. Li, J. Xu, X. Wang, Superior adsorption capacity of hierarchical iron oxide@magnesium silicate magnetic nanorods for fast removal of organic pollutants from aqueous solution, *J. Mater. Chem. A* 1 (2013) 11691–11697, <https://doi.org/10.1039/c3ta12767b>.
- K.Y. Jung, K.H. Han, Y.C. Kang, H.K. Jung, Preparation of CaMgSi<sub>2</sub>O<sub>6</sub>:Eu blue phosphor particles by spray pyrolysis and its VUV characteristics, *Mater. Chem. Phys.* 98 (2006) 330–336, <https://doi.org/10.1016/j.matchemphys.2005.09.032>.
- K.Y. Jung, J.H. Kim, Y.C. Kang, Luminescence enhancement of Eu-doped calcium magnesium silicate blue phosphor for UV-LED application, *J. Lumin.* 129 (2009) 615–619, <https://doi.org/10.1016/j.jlumin.2009.01.001>.
- A. Bigham, S.A. Hassanzadeh-Tabrizi, M. Rafieini, H. Salehi, Ordered mesoporous magnesium silicate with uniform nanochannels as a drug delivery system: the effect of calcination temperature on drug delivery rate, *Ceram. Int.* 42 (2016) 17185–17191, <https://doi.org/10.1016/j.ceramint.2016.08.009>.
- T.W. Sun, Y.J. Zhu, C. Qi, F. Chen, Y.Y. Jiang, Y.G. Zhang, J. Wu, C. Wu, Templated solvothermal synthesis of magnesium silicate hollow nanospheres with ultrahigh specific surface area and their application in high-performance protein adsorption and drug delivery, *J. Mater. Chem. B* 4 (2016) 3257–3268, <https://doi.org/10.1039/c5tb02632f>.
- W. Zhai, H. Lu, L. Chen, X. Lin, Y. Huang, K. Dai, K. Naoki, G. Chen, J. Chang, Silicate bioceramics induce angiogenesis during bone regeneration, *Acta Biomater.* 8 (2012) 341–349, <https://doi.org/10.1016/j.actbio.2011.09.008>.
- K.P. Sanosh, A. Balakrishnan, L. Francis, T.N. Kim, Sol-gel synthesis of forsterite nanopowders with narrow particle size distribution, *J. Alloys Compd.* 495 (2010) 113–115, <https://doi.org/10.1016/j.jallcom.2010.01.097>.
- S. Ni, L. Chou, J. Chang, Preparation and characterization of forsterite (Mg<sub>2</sub>SiO<sub>4</sub>) bioceramics, *Ceram. Int.* 33 (2007) 83–88, <https://doi.org/10.1016/j.ceramint.2005.07.021>.
- M. Karaihia, M.H. Fathi, Synthesis and characterization of bioactive forsterite nanopowder, *Ceram. Int.* 35 (2009) 2449–2454, <https://doi.org/10.1016/j.ceramint.2009.02.001>.
- J. Zhang, L. Dang, M. Zhang, Q. Lu, S. Zhao, Characterization of mesoporous magnesium silicate with hierarchical structure and its adsorption performance for dye and lead ion, *Surf. Interfaces* 8 (2017) 112–118, <https://doi.org/10.1016/j.surfin.2017.05.005>.
- V. Šepelák, S. Bégin-Colin, G. Le Caer, Transformations in oxides induced by high-energy ball-milling, *Dalton Trans.* 41 (2012) 11927–11948, <https://doi.org/10.1039/c2dt30349c>.
- F. Tavangarian, R. Emadi, Mechanical activation assisted synthesis of pure nanocrystalline forsterite powder, *J. Alloys Compd.* 485 (2009) 648–652, <https://doi.org/10.1016/j.jallcom.2009.06.051>.
- F. Tavangarian, R. Emadi, Synthesis of nanocrystalline forsterite (Mg<sub>2</sub>SiO<sub>4</sub>) powder by combined mechanical activation and thermal treatment, *Mater. Res. Bull.* 45 (2010) 388–391, <https://doi.org/10.1016/j.materresbull.2009.12.032>.
- M.T. Tsai, Synthesis of nanocrystalline enstatite fiber via alkoxide sol-gel process, *J. Am. Ceram. Soc.* 88 (2005) 1770–1772, <https://doi.org/10.1111/j.1551-2916.2005.00359.x>.
- M.E. Song, J.S. Kim, M.R. Joung, S. Nahm, Y.S. Kim, J.H. Paik, B.H. Choi, Synthesis and microwave dielectric properties of MgSiO<sub>3</sub> ceramics, *J. Am. Ceram. Soc.* 91 (2008) 2747–2750, <https://doi.org/10.1111/j.1551-2916.2008.02499.x>.
- Y. Zhuang, Y. Yang, G. Xiang, X. Wang, Magnesium silicate hollow nanostructures as highly efficient absorbents for toxic metal ions, *J. Phys. Chem. C* 113 (2009) 10441–10445, <https://doi.org/10.1021/jp9014756>.
- B. Wang, Q.Y. Chang, K. Gao, H.R. Fang, T. Qing, N.N. Zhou, The synthesis of magnesium silicate hydroxide with different morphologies and the comparison of

their tribological properties, *Tribol. Int.* 119 (2018) 672–679, <https://doi.org/10.1016/j.triboint.2017.11.020>.

[45] F. Dellisanti, G. Valdré, On the high-temperature structural behaviour of talc (Mg3Si 4O10(OH)2) to 1600C: effect of mechanical deformation and strain, *Philos. Mag. A* 90 (2010) 2443–2457, <https://doi.org/10.1080/14786431003772991>.

[46] O.Y. Golubeva, E.N. Korytkova, V.V. Gusarov, Hydrothermal synthesis of magnesium silicate montmorillonite for polymer-clay nanocomposites, *Russ. J. Appl. Chem.* 78 (2005) 26–32, <https://doi.org/10.1007/s11167-005-0225-z>.

[47] Z.A. Alothman, A review: fundamental aspects of silicate mesoporous materials, *Materials* 5 (2012) 2874–2902, <https://doi.org/10.3390/ma5122874>.

[48] X.S. Zhao, G.Q. Lu, G.J. Millar, Advances in mesoporous molecular sieve MCM-41, *Ind. Eng. Chem. Res.* 35 (1996) 2075–2090, <https://doi.org/10.1021/ie950702a>.

[49] C. Perego, R. Millinib, Porous materials in catalysis: challenges for mesoporous materials, *Chem. Soc. Rev.* 42 (2013) 3956–3976, <https://doi.org/10.1039/c2cs35244c>.

[50] F. Di Renzo, A. Galarneau, P. Trens, F. Fajula, Micelle-Templated Materials, *Handb. Porous Solids*, 2002, pp. 1311–1395, <https://doi.org/10.1002/9783527618286.ch21a>.

[51] Q. Lu, Q. Li, J. Zhang, J. Li, J. Lu, Facile mesoporous template-assisted hydrothermal synthesis of ordered mesoporous magnesium silicate as an efficient adsorbent, *Appl. Surf. Sci.* 360 (2016) 889–895, <https://doi.org/10.1016/j.apsusc.2015.11.081>.

[52] Y. Zhu, D. Jian, S. Wang, Synthesis of mesoporous magnesium silicate particles and their adsorption property, *Micro & Nano Lett.* 6 (2011) 671–674, <https://doi.org/10.1049/mnl.2011.0265>.

[53] H. Tüysüz, F. Schüth, Ordered mesoporous materials as catalysts, 2012, <https://doi.org/10.1016/B978-0-12-385516-9.00002-8>.

[54] J.N. Kondo, K. Domon, Crystallization of mesoporous metal oxides, *Chem. Mater.* 20 (2008) 835–847, <https://doi.org/10.1021/cm702176m>.

[55] S. Jun, Sang Hoon Joo, R. Ryoo, M. Kruk, M. Jaroniec, Z. Liu, T. Ohsuna, O. Terasaki, Synthesis of new, nanoporous carbon with hexagonally ordered mesostructure [5], *J. Am. Chem. Soc.* 122 (2000) 10712–10713, <https://doi.org/10.1021/ja002261e>.

[56] J. Ilavsky, F. Zhang, A.J. Allen, L.E. Levine, P.R. Jemian, G.G. Long, Ultra-small-angle X-ray scattering instrument at the advanced photon source: history, recent development, and current status, *Metall. Mater. Trans. A. Phys. Metall. Mater. Sci.* 44 (2013) 68–76, <https://doi.org/10.1007/s11661-012-1431-y>.

[57] U. Bonse, M. Hart, Tailless x-ray single-crystal reflection curves obtained by multiple reflection, *Appl. Phys. Lett.* 7 (1965) 238–240, <https://doi.org/10.1063/1.1754396>.

[58] O.H. Teresa, C.K. Choi, Comparison between SiOC thin films fabricated by using plasma enhance chemical vapor deposition and SiO2 thin films by using fourier transform infrared spectroscopy, *J. Kor. Phys. Soc.* 56 (2010) 1150–1155, <https://doi.org/10.3938/jkps.56.1150>.

[59] S. Grangeon, F. Claret, C. Roosz, T. Sato, S. Gaboreau, Y. Linard, Structure of nanocrystalline calcium silicate hydrates: insights from X-ray diffraction, synchrotron X-ray absorption and nuclear magnetic resonance, *J. Appl. Crystallogr.* 49 (2016) 771–783, <https://doi.org/10.1107/S1600576716003885>.

[60] P. Post, L. Wurlitzer, W. Maus-Friedrichs, A.P. Weber, Characterization and applications of nanoparticles modified in-flight with silica or silica-organic coatings, *Nanomaterials* 8 (2018) 1–19, <https://doi.org/10.3390/nano8070530>.

[61] L.M. Johnson, L. Gao, C.W. Shields, M. Smith, K. Efimenco, K. Cushing, J. Genzer, G.P. López, Elastomeric microparticles for acoustic mediated biopreparations, *J. Nanobiotechnol.* 11 (2013) 1–8, <https://doi.org/10.1186/1477-3155-11-22>.

[62] S. Mušić, N. Filipović-Vinceković, L. Sekovanić, Precipitation of amorphous SiO2 particles and their properties, *Braz. J. Chem. Eng.* 28 (2011) 89–94, <https://doi.org/10.1590/S0104-6632201100010011>.

[63] C. Vancea, M. Mihailescu, A. Negrea, G. Mosoarca, M. Ciopec, N. Duteanu, P. Negrea, V. Minzatu, Batch and fixed-bed column studies on palladium recovery from acidic solution by modified mgsio3, *Int. J. Environ. Res. Publ. Health* 17 (2020) 1–17, <https://doi.org/10.3390/ijerph17249500>.

[64] C. Karlsson, E. Zanghellini, J. Swenson, B. Roling, D.T. Bowron, L. Börjesson, Structure of mixed alkali/alkaline-earth silicate glasses from neutron diffraction and vibrational spectroscopy, *Phys. Rev. B Condens. Matter* 72 (2005) 1–12, <https://doi.org/10.1103/PhysRevB.72.064206>.

[65] H. Asgar, V. Semeykina, M. Hunt, S. Mohammed, I. Kuzmenko, I. Zharov, G. Gadikota, Thermally-Induced morphological evolution of spherical silica nanoparticles using in-operando X-ray scattering measurements, *Colloids Surf. A Physicochem. Eng. Asp.* 586 (2020), <https://doi.org/10.1016/j.colsurfa.2019.124260>.

[66] H. Asgar, S. Seifert, I. Kuzmenko, M. Bartl, G. Gadikota, Mechanistic insights into the colloidal assembly of mesoporous silica using in-operando cross-scale X-ray scattering and spectroscopic measurements, *Materialia* 12 (2020), 100764.

[67] K. Kim, J. Kim, W. Kim, Influence of reaction conditions on sol-precipitation process producing silicon oxide particles, *Ceram. Int.* 28 (2002) 187–194.

[68] C.J. Brinker, G.W. Scherer, *Sol-Gel Science: the Physics and Chemistry of Sol-Gel Processing*, Academic Press, San Diego, 1990.

[69] F. Azimov, I. Markova, V. Stefanova, K. Sharipov, Synthesis and characterization of SBA-15 AND Ti-SBA-15 nanoporous materials for DME catalysts, *J. Univ. Chem. Technol. Metall.* 47 (2012) 333–340.

[70] Y. Song, L.Y. Yang, Y. guang Wang, D. Yu, J. Shen, X. kun Ouyang, Highly efficient adsorption of Pb(II) from aqueous solution using amino-functionalized SBA-15/calcium alginate microspheres as adsorbent, *Int. J. Biol. Macromol.* 125 (2019) 808–819, <https://doi.org/10.1016/j.ijbiomac.2018.12.112>.

[71] A.M. Escatlar, T. Lazaukas, S.M. Woodley, S.T. Bromley, Structure and properties of nanosilicates with olivine (Mg2 SiO4)N and pyroxene (MgSiO3)N compositions, *ACS Earth Sp. Chem.* 3 (2019) 2390–2403, <https://doi.org/10.1021/acsearthspacechem.9b00139>.

[72] S.S. Physics, F.S.U. Jena, Steps toward interstellar silicate mineralogy. V. Thermal evolution of amorphous magnesium silicates and silica, *Astron. Astrophys.* 364 (2000) 282–292.

[73] I. Prasad, A.N. Chandorkar, Spectroscopy of silicon dioxide films grown under negative corona stress, *J. Appl. Phys.* 94 (2003) 2308–2310, <https://doi.org/10.1063/1.1593222>.

[74] P. Innocenzi, P. Falcaro, D. Grossi, F. Babonneau, Order-disorder transitions and evolution of silica structure in self-assembled mesostructured silica films studied through FTIR spectroscopy, *J. Phys. Chem. B* 107 (2003) 4711–4717, <https://doi.org/10.1021/jp026609z>.

[75] M. Ghoorah, B.Z. Dlugogorski, H.C. Oskierski, E.M. Kennedy, Study of thermally conditioned and weak acid-treated serpentinites for mineralisation of carbon dioxide, *Miner. Eng.* 59 (2014) 17–30, <https://doi.org/10.1016/j.mine.2014.02.005>.

[76] L. Sharma, R. Kakkar, Hierarchical porous magnesium oxide (Hr-MgO) microspheres for adsorption of an organophosphate pesticide: kinetics, isotherm, thermodynamics, and DFT studies, *ACS Appl. Mater. Interfaces* 9 (2017) 38629–38642, <https://doi.org/10.1021/acsami.7b14370>.

[77] E. Talik, W. Zarek, M. Kruczak, S. Ganschow, D. Skrzypek, E. Popiel, Characterization of olivine single crystals grown by the micro-pulling-down method and terrestrial olivine by XPS, Mössbauer, magnetic and EPR methods, *Cryst. Res. Technol.* 41 (2006) 979–987, <https://doi.org/10.1002/crat.200610708>.

[78] R. Gustus, W. Gruber, L. Wegewitz, U. Geckle, R. Prang, C. Kübel, H. Schmidt, W. Maus-Friedrichs, Decomposition of amorphous Si2C by thermal annealing, *Thin Solid Films* 552 (2014) 232–240, <https://doi.org/10.1016/j.thinsof.2013.12.033>.

[79] L. Kang, J. Gao, H.R. Xu, S.Q. Zhao, H. Chen, P.H. Wu, Epitaxial Mg2SiO4 thin films with a spinel structure grown on Si substrates, *J. Cryst. Growth* 297 (2006) 100–104, <https://doi.org/10.1016/j.jcrysgr.2006.09.036>.

[80] V.P. Zakaznova-Herzog, H.W. Nesbitt, G.M. Bancroft, J.S. Tse, X. Gao, W. Skinner, High-resolution valence-band XPS spectra of the nonconductors quartz and olivine, *Phys. Rev. B Condens. Matter* 72 (2005) 1–13, <https://doi.org/10.1103/PhysRevB.72.205113>.

[81] Z. Li, Y. Yuan, X. Jing, Effect of current density on the structure, composition and corrosion resistance of plasma electrolytic oxidation coatings on Mg-Li alloy, *J. Alloys Compd.* 541 (2012) 380–391, <https://doi.org/10.1016/j.jallcom.2012.06.139>.

[82] J.S. Corneille, J. He, D.W. Goodman, *MgO XPS*, 1994, p. 6028.

[83] X. Zhu, D. Wu, W. Wang, F. Tan, P.K. Wong, X. Wang, X. Qiu, X. Qiao, Highly effective antibacterial activity and synergistic effect of Ag-MgO nanocomposite against Escherichia coli, *J. Alloys Compd.* 684 (2016) 282–290, <https://doi.org/10.1016/j.jallcom.2016.05.179>.

[84] Y. Zhang, L. Zhu, L. Chen, L. Liu, G. Ye, Influence of magnesia on demoulding strength of colloidal silica-bonded castables, *Rev. Adv. Mater. Sci.* 58 (2019) 32–37, <https://doi.org/10.1515/rams-2019-0008>.

[85] B.P. Vinayan, Z. Zhao-Karger, T. Diemant, V.S.K. Chakravadhanula, N. I. Schwarburger, M.A. Cambaz, R.J. Behm, C. Kübel, M. Fichtner, Performance study of magnesium-sulfur battery using a graphene based sulfur composite cathode electrode and a non-nucleophilic Mg electrolyte, *Nanoscale* 8 (2016) 3296–3306, <https://doi.org/10.1039/c5nr04383b>.

[86] D. Yang, A. Velamakanni, G. Bozoklu, S. Park, M. Stoller, R.D. Piner, S. Stankovich, I. Jung, D.A. Field, C.A. Ventrice, R.S. Ruoff, Chemical analysis of graphene oxide films after heat and chemical treatments by X-ray photoelectron and Micro-Raman spectroscopy, *Carbon* 49 (2009) 145–152, <https://doi.org/10.1016/j.carbon.2008.09.045>.

[87] T.L. Barr, The nature of the relative bonding chemistry in zeolites: an XPS study, *Zeolites* 10 (1990) 760–765, [https://doi.org/10.1016/0144-2449\(90\)90058-Y](https://doi.org/10.1016/0144-2449(90)90058-Y).

[88] S. Evans, Correction for the effects of adventitious carbon overlayers in quantitative XPS analysis, *Surf. Interface Anal.* 25 (1997) 924–930, [https://doi.org/10.1002/\(SICI\)1096-9918\(199711\)25:12<924::AID-SIA317>3.0.CO\\_2-2](https://doi.org/10.1002/(SICI)1096-9918(199711)25:12<924::AID-SIA317>3.0.CO_2-2).

[89] L. Chen, Z. Xu, J. Li, B. Zhou, M. Shan, Y. Li, L. Liu, B. Li, J. Niu, Modifying graphite oxide nanostructures in various media by high-energy irradiation, *RSC Adv.* 4 (2014) 1025–1031, <https://doi.org/10.1039/c3ra46203>.

[90] V.G. Tsirelson, A.S. Avilov, Y.A. Abramov, E.L. Belokoneva, R. Kitaneh, D. Feil, X-ray and electron diffraction study of MgO, *Acta Crystallogr. Sect. B Struct. Sci.* 54 (1998) 8–17, <https://doi.org/10.1107/S0108768197008963>.

[91] R.K. Biswas, P. Khan, S. Mukherjee, A.K. Mukhopadhyay, J. Ghosh, K. Muraleedharan, Study of short range structure of amorphous Silica from PDF using Ag radiation in laboratory XRD system, Raman and NEXAFS, *J. Non-Cryst. Solids* 488 (2018) 1–9, <https://doi.org/10.1016/j.jnoncrysol.2018.02.037>.

[92] S. Speakman, Estimating crystallite size using XRD (MIT center for materials science and engineering, estim. Cryst. Size using XRD, MIT Cent. Mater. Sci. Eng. (2008) 5–15.

[93] X. Li, X. Lian, F. Liu, Rear-end road crash characteristics analysis based on Chinese in-depth crash study data, *CICTP 2016 - green multimodal transp. Logist. - Proc. 16th COTA Int. Conf. Transp. Prof.* (2016) 1536–1545, <https://doi.org/10.1061/9780784479896.140>.

[94] K. Sangwal, K. Ramakrishna Rao, A note on the dissolution mechanism of MgO crystals in acids, *J. Mater. Sci.* 15 (1980) 2673–2675, <https://doi.org/10.1007/BF00550779>.

[95] J.R. Smyth, R.M. Hazen, The crystal structures of forsterite and hortonolite at several temperatures up to 900 °C, *Am. Mineral.* 58 (1973) 588–593.

[96] R.M. Hazen, Effects of temperature and pressure on the cell dimension and X-ray temperature factors of periclase, *Am. Mineral.* 61 (1976) 266–271.

[97] H. Yang, S. Ghose, High temperature single crystal X-ray diffraction studies of the ortho-proto phase transition in enstatite,  $Mg_2Si_2O_6$  at 1360 K, *Phys. Chem. Miner.* 22 (1995) 300–310, <https://doi.org/10.1007/BF00202770>.

[98] D. Zhao, J. Feng, Q. Huo, N. Melosh, G.H. Fredrickson, B.F. Chmelka, G.D. Stucky, Triblock copolymer syntheses of mesoporous silica with periodic 50 to 300 angstrom pores, *Science* (80-.) 279 (1998) 548–552, <https://doi.org/10.1126/science.279.5350.548>.

[99] M. Thommes, B. Smarsly, M. Groenewolt, P.I. Ravikovich, A.V. Neimark, Adsorption hysteresis of nitrogen and argon in pore networks and characterization of novel micro- and mesoporous silicas, *Langmuir* 22 (2006) 756–764, <https://doi.org/10.1021/la051686h>.

[100] J. Landers, G.Y. Gor, A.V. Neimark, Density functional theory methods for characterization of porous materials, *Colloids Surf. A Physicochem. Eng. Asp.* 437 (2013) 3–32, <https://doi.org/10.1016/j.colsurfa.2013.01.007>.

[101] A.V. Neimark, Y. Lin, P.I. Ravikovich, M. Thommes, Quenched solid density functional theory and pore size analysis of micro-mesoporous carbons, *Carbon N.Y.* 47 (2009) 1617–1628, <https://doi.org/10.1016/j.carbon.2009.01.050>.

[102] M. Thommes, K. Kaneko, A.V. Neimark, J.P. Olivier, F. Rodrigues-Reinoso, J. Rouquerol, K.S.W. Sing, Physisorption of gases, with special reference to the evaluation of surface area and pore size distribution (IUPAC Technical Report), *Pure Appl. Chem.* 87 (2015) 1051–1069.

[103] F. Rouquerol, J. Rouquerol, K. Sing, *Adsorption by Powders and Porous Solids*, Academic Press, London, 1999.

[104] T. Kjellman, N. Reichhardt, M. Sakeye, J.H. Smałšt, M. Lindén, V. Alfredsson, Independent fine-tuning of the intrawall porosity and primary mesoporosity of SBA-15, *Chem. Mater.* 25 (2013) 1989–1997, <https://doi.org/10.1021/cm4009442>.

[105] Y. Zhao, S. Sun, X. Cai, Y. Fan, W. Jiang, B. Zhou, S. Gu, N. Shi, W. Luo, L. Wang, Enhancement in sintering driving force derived from in situ ordered structural collapse of mesoporous powders, *J. Am. Ceram. Soc.* 103 (2020) 5654–5663, <https://doi.org/10.1111/jace.17343>.